

# Unshifted Metastable He I\* Mini-Broad Absorption Line System in the Narrow Line Type 1 Quasar SDSS J080248.18+551328.9

Tuo Ji<sup>1,2,3</sup>, Hongyan Zhou<sup>1,2,3</sup>, Peng Jiang<sup>2,3,1</sup>, Tinggui Wang<sup>2,3,1</sup>, Jian Ge<sup>4</sup>,  
Huiyuan Wang<sup>2,3,1</sup>, S. Komossa<sup>5,6,7</sup>, Fred Hamann<sup>4</sup>, Jens Zuther<sup>8</sup>, Wenjuan Liu<sup>1,2,3</sup>,  
Honglin Lu<sup>2,3</sup>, Wenwen Zuo<sup>9</sup>, Chenwei Yang<sup>1,2,3</sup>, and Weimin Yuan<sup>5,10</sup>

## ABSTRACT

We report the identification of an unusual absorption line system in the quasar SDSS J080248.18+551328.9 and present a detailed study of the system, incorporating follow-up optical and NIR spectroscopy. A few tens of absorption lines are detected, including He I\*, Fe II\* and Ni II\* that arise from metastable or excited levels, as well as resonant lines in Mg I, Mg II, Fe II, Mn II, and Ca II. All of the isolated absorption lines show the same profile of width  $\Delta v \sim 1,500 \text{ km s}^{-1}$  centered at a common redshift as that of the quasar emission lines, such as [O II], [S II], and hydrogen Paschen and Balmer series. With narrow Balmer lines, strong optical Fe II multiplets, and weak [O III] doublets, its emission line spectrum is typical for that of a narrow-line Seyfert 1 galaxy (NLS1). We have derived reliable measurements of the gas-phase column densities of the absorbing ions/levels. Photoionization modeling indicates that the absorber has a density of  $n_{\text{H}} \sim (1.0 - 2.5) \times 10^5 \text{ cm}^{-3}$  and a column density of  $N_{\text{H}} \sim (1.0 - 3.2) \times 10^{21} \text{ cm}^{-2}$ , and is located at  $R \sim 100 - 250 \text{ pc}$  from the central super-massive black hole. The location of the absorber, the symmetric profile of the absorption lines, and the coincidence of the absorption and emission line centroid jointly suggest that the absorption gas is originated from the host galaxy and is plausibly accelerated by stellar processes, such as stellar winds and/or supernova explosions. The implications for the detection of such a peculiar absorption line system in an NLS1 are discussed in the context of co-evolution between super-massive black hole growth and host galaxy build-up.

*Subject headings:* quasars: absorption lines – quasars: emission lines – quasars: individual (SDSS J080248.18+551328.9)

<sup>1</sup>Polar Research Institute of China, 451 Jinqiao Road, Pudong, Shanghai 200136, China, jituo@pric.gov.cn

<sup>2</sup>Key Laboratory for Research in Galaxies and Cosmology, The University of Science and Technology of China, Chinese Academy of Sciences, Hefei, Anhui, 230026, China

<sup>3</sup>Center for Astrophysics, University of Science and Technology of China, Hefei, Anhui, 230026, China

<sup>4</sup>Department of Astronomy, University of Florida, Gainesville, FL 3261, US

<sup>5</sup>National Astronomical Observatories, Chinese Academy of Sciences, 20A Datun Road, Beijing, 100012, China

<sup>6</sup>Excellence Cluster Universe, Technische Universitaet Muenchen, Boltzmannstrasse 2, 85748 Garching, Germany

<sup>7</sup>Max-Planck-Institut fuer Radioastronomie, Auf dem Huegel 69, 53121 Bonn, Germany

<sup>8</sup>Physikalisches Institut, Universität zu Köln, Zùlpicher

## 1. Introduction

It is now generally believed that active galactic nuclei (AGNs), including their high-luminosity analog quasars, are powered by a super-massive black hole (SMBH) fed by accretion flows. To enable the fuel feeding process, the angular momentum of the interstellar gas in the central

Strasse 77, 50937 Köln, Germany

<sup>9</sup>Department of Astronomy, Peking University, Beijing 100871, China

<sup>10</sup>National Astronomical Observatories/Yunnan Observatory and Key Laboratory of the Structure and Evolution of Celestial Objects, Chinese Academy of Sciences, Kunming 650011, China

region of host galaxy must be largely removed to bring the gaseous fuel into the nuclear region. None-axisymmetric perturbation of gravitational potential, such as that due to stellar bars and interaction with companion galaxies, are proven to be efficient ways to drive large amounts of gas inwards on spatial scale of kpcs and at timescales of Gyrs (Wada 2004; Davies 2009). However, molecular mappings of nearby Seyferts (e.g. NGC 1068, Müller Sánchez et al. 2009; NGC 1097, Davies et al. 2009), show that the gas inflow is terminated at spatial scales of a few to tens of pcs. Other mechanisms, rather than gravity, are necessary to drive the circumnuclear inflows. Theoretically, the stalled molecular gas will definitely result in nuclear starbursts (Hicks et al. 2009). The energetic stellar processes of circumnuclear starburst might funnel gas further inwards to intra-pc scale to fuel the black hole accretion (Davies et al. 2007; Schartmann et al. 2009).

The fueling processes should manifest themselves more observable in AGNs with high mass accretion rate. A sub-class of AGNs, namely narrow-line Seyfert 1 galaxies (NLS1s)<sup>1</sup>, are generally considered to be AGNs at their early evolutionary stage with small black hole masses accreting at very close to the maximum allowed accretion rate (see Komossa 2008 for an extensive review). They are traditionally defined by the narrowness of their Balmer emission lines ( $\text{FWHM}_{\text{H}\beta} < 2000 \text{ km s}^{-1}$ ) and weakness of [O III] emission ( $[\text{O III}]/\text{H}\beta < 3$ ; Osterbrock & Pogge 1985, but see also Zhou et al. 2006b for a slightly different definition). Strong Fe II emission is also a significant feature for NLS1s.

Mathur (2000) suggested that NLS1s live in gas-rich galaxies with ongoing star formation. Observationally, star formation in the host galaxies of NLS1s is considerable stronger compared with that of the normal type 1 AGNs using Spitzer mid-infrared spectroscopy (Sani et al. 2010). The observations can be merged into the scenario of co-evolution of galaxy and central black hole (e.g. Granato et al. 2004). The energetic stellar pro-

cesses of circumnuclear starburst might induce the surrounding gas flowing inwards more efficiently to trigger high activity of the central black hole (Davies et al. 2007; Schartmann et al. 2009). Provided that the gaseous inflows would occasionally intercept our line of sight toward active nucleus, they can be observable through quasar absorption line technique.

In this paper, we report the first such candidate absorption line system toward the narrow line type 1 quasar SDSS J080248.18+551328.9 (hereafter SDSS J0802+5513 for brevity), and present detailed study of the system incorporating follow-up optical and NIR spectroscopy.

SDSS J0802+5513 was initially identified as a quasar during the Sloan Digital Sky Survey (SDSS, York et al. 2000) based on spectroscopic observation on 2003-03-24, and was included in the SDSS quasar catalogue with a redshift of  $z = 0.6640 \pm 0.0005$  (Schneider et al. 2007, 2010). It was first classified as a low-ionization broad absorption line (LoBAL) quasar by Gibson et al. (2009) according to detection of Mg II broad absorption trough with width  $\Delta v \approx 2,500 \text{ km s}^{-1}$ . The authors also reported possible detection of Fe II  $\lambda\lambda 2414, 2632, 2750$  absorption lines. SDSS J0802+5513 was later analyzed by Zhang et al. (2010) but rejected as a LoBAL quasar since the Mg II absorption line does not show a large enough blueshift, though the absorption trough is broader than their threshold value of  $\Delta v > 1,600 \text{ km s}^{-1}$ . Using Kohonen self-organizing maps, Meusinger et al. (2012) again classified SDSS J0802+5513 as an unusual LoBAL quasar with a red color and narrow absorption line troughs, and confirmed the classification by visual inspection of its SDSS spectrum. The discrepant classification of the absorption lines in the quasar deserves further exploration.

We noticed SDSS J0802+5513 during our systematic search for He I\*  $\lambda\lambda 2765, 2830, 2946, 3189, 3889, 10830$  absorption multiplets in quasars<sup>2</sup> (Liu et al. 2014, submitted to ApJS). Arising from the common metastable He I\*  $2^3\text{S}$  level, the multiplets are rarely seen in the interstellar medium

<sup>1</sup> Following Komossa et al. (2006), we collectively speak of NLS1s when referring to the class properties of narrow line Seyfert 1 galaxies and narrow line type 1 quasars; and we distinguish between a Seyfert galaxy and a quasar according to the classical criterion of B-band absolute magnitude when referring to individual objects.

<sup>2</sup>In this paper, we will use ‘\*’ to denote absorption lines that arise from metastable/excited levels. E.g., metastable neutral helium absorption lines will be referred to as He I\*, and singly-ionized iron absorption lines from excited levels as Fe II\*.

of normal galaxies (Rudy et al. 1985). The  $2^3\text{S}$  level is mainly populated by recombination of  $\text{He}^+$ . With an ionization potential of 4.8 eV, the diffuse stellar radiation background can easily ionize helium atoms at the  $2^3\text{S}$  level, while lacking of enough hard photons of  $h\nu > 24.59$  eV to ionize helium atoms at the ground level. Whereas quasar continuum is energetic enough to populate a large number of He atoms at the  $2^3\text{S}$  level. He I\* multiplets are hence a good indicator for distinguishing quasar intrinsic narrow absorption lines (NAL) from intervening NALs that are physically unrelated to the background quasars, in complementary to the two often used indicators (e.g. Hamann et al. 1997; Misawa et al. 2003): (1) time variability and (2) partially coverage of the absorption lines. He I\* multiplets are very useful for determining the covering factor of quasar absorption gas due to the large oscillator strength differences in the multiplets. This, together with their common highly metastable lower transition  $2^3\text{S}$  level<sup>3</sup>, endue He I\* multiplets with a high sensitivity to a large dynamic range of column densities when other strong UV resonant lines, such as O VI, N V, C IV, Si IV, Al III and Mg II, are heavily saturated (Arav et al. 2001b; Leighly et al. 2011, 2014). The wide wavelength separations of the lines in He I\* multiplets also relieve line blending, which is always a severe problem for BAL studies. Clear detection of He I\*  $\lambda\lambda 3189, 3889, 10830$  and a few tens of other absorption lines, including Ni II\*, Fe II\*, Fe II, Mn II, Ca II, Mg II and Mg I, enable us to derive reliable measurements of the column densities of the corresponding ions/levels; to probe the physical conditions of the absorption gas; and to locate the gas with the aid of photoionization model calculations.

The paper is organized as follows. In §2, we will present a brief description of the SDSS quasar sample with He I\* absorption line multiplets, and identify SDSS J0802+5513 as an outlier in the sample. We will also describe there the data used in this paper, including collection of archived data and observations and data reductions of our new spectroscopies. Measurements of emission and

absorption lines will be presented in §3. In §4, we will perform extensive photoionization simulations with the spectral synthesis code CLOUDY (Ferland et al. 1998), and make comparison between model calculations and absorption line measurements. Possible origin of the absorption gas and its implications will be discussed in §5. Our main results will be summarized in the last section, together with future perspectives. Throughout this paper, we assume a cosmology with  $\Omega_\Lambda = 0.7$ ,  $\Omega_M = 0.3$ , and  $H_0 = 70 \text{ km s}^{-1} \text{ Mpc}^{-1}$ . All quoted magnitudes are using AB-system except 2MASS ones, which are Vega magnitudes. We use negative velocities to denote blueshifted absorption lines, and positive values for redshifted lines.

## 2. Identification, Observations and Data Reduction

### 2.1. SDSS J0802+5513 as an Outlier of Quasar He I\* Absorbers

He I\* multiplets are much under-explored as an important diagnostics for the ionization state of quasar absorption gas. So far only a handful detections have been reported in the literature (see Liu et al. 2014 for a summarization). He I\*  $\lambda 10830$ , located in the NIR and the strongest line in the multiplets, is beyond the wavelength coverage of most large sky area optical spectroscopic surveys. With a  $\lambda f_{ik}$  value of 23.3 times less than He I\*  $\lambda 10830$  (Leighly et al. 2011), the second strongest line, He I\*  $\lambda 3889$ , though falling in the optical for quasars at  $z \lesssim 1$ , is much weaker than those familiar UV resonant lines. In that wavelength range, the pseudo-continuum from complex iron multiplets, which usually varies a lot from object to object, makes the normalization quite uncertain. Detection of such a weak line with contamination is a challenging task. We developed a new detection technique to minimize the uncertainty of normalization. We use the observed quasar spectra in a selected library to mimic the absorption free spectra of the quasar of interest, in analog to the pair-method traditionally used to recover the extinction-free stellar spectra (see Liu et al. 2014 for a full description of the method). The ‘pair-method’ can yield a much better precision than the often-adopted approaches for quasar absorption line measurements. Using this newly developed technique, we detected

<sup>3</sup> The asymptotic maximum value of  $n_{2^3\text{S}}/n_{\text{He}^+} \approx 10^6$  for a temperature of  $10^4$  K and an electron density of  $n_e \gtrsim 10^4 \text{ cm}^{-3}$  when collisional de-excitation rate dominates radiative rate (Rudy 1985).

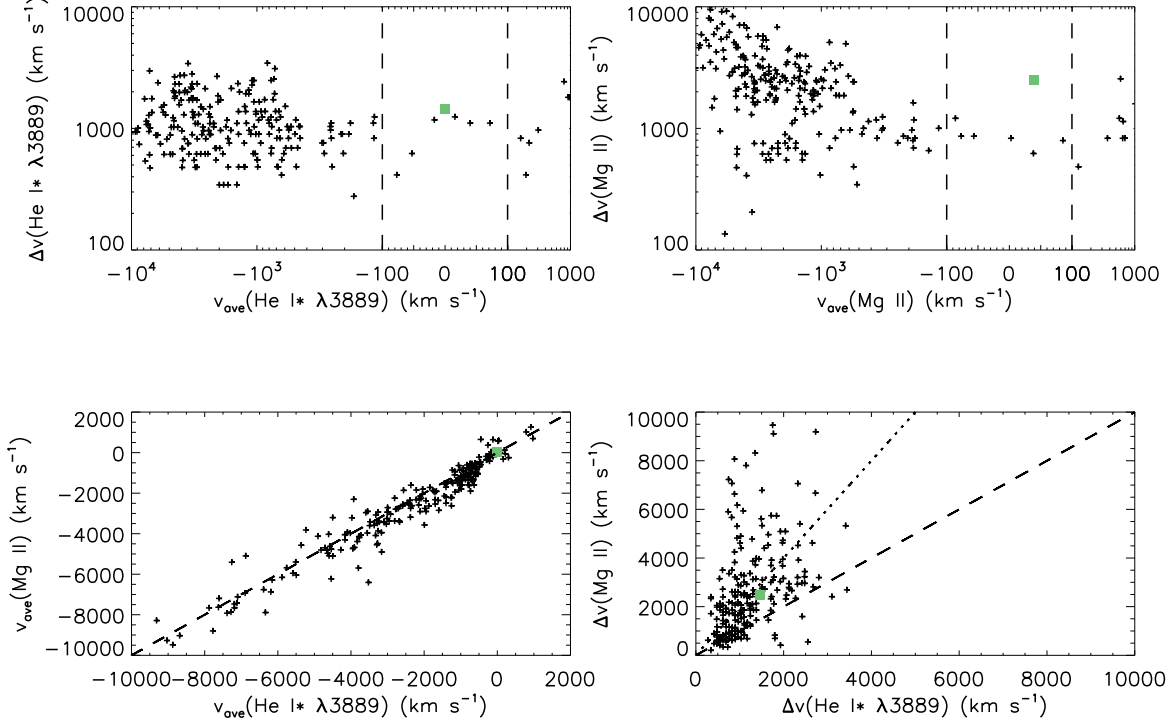


Fig. 1.— Upper left: He I\*  $\lambda 3889$  absorption line velocity shifts  $v_{\text{ave}}$  versus their widths  $\Delta v$  for quasar He I\* absorbers identified from SDSS DR7. For absorbers with  $|v| > 100$ , abscissa is in log scale, while for absorbers with  $|v| < 100$  in linear scale. SDSS J0802+5513 is shown as a green square. Two vertical dashed lines at  $\pm 100 \text{ km s}^{-1}$  are shown to guide the eyes. Absorbers in between the two vertical lines are deemed as unshifted, for the dispersion is in agreement with uncertainties of systematic redshift determination for SDSS quasars. Upper right: same as upper left except for Mg II lines. The velocity and width of the two lines are compared in the lower two panels (lower left: velocity, lower right: width). Note that the velocities of the two lines almost have the same values as indicated by the dashed line, while the widths of Mg II are much larger than that of He I (Mg II:He I=1:1 and 1:2 are shown as dashed and dotted lines, respectively, to guide the eyes).

He I\*  $\lambda 3889$  line at  $> 2 \sigma$  confidence level in 247 quasars with Mg II absorption from the Seventh Data Release (DR7) of SDSS. The quoted uncertainties include both statistical and systematic errors. As shown in Figure 1, the velocity centroid of Mg II and He I\*  $\lambda 3889$  agrees with each other within 10%. This indicates that the vast majority of absorption lines in the sample are real detections, since Mg II and He I\*  $\lambda 3889$  are measured independently. In this Figure, we also compared the width of Mg II and He I\*  $\lambda 3889$ , and found that the former is on average 2 times broader than

the later with a rather large scatter. This fact was also noted by Arav et al. (2001b) in a case study of QSO 2359–1241.

The sample show interesting pattern in the Mg II line velocity against width ( $v_{\text{ave}} - \Delta v$ )<sup>4</sup> plane of Figure 1. Line width is strongly correlated with velocity for absorbers in the upper-left corner ( $\Delta v$  and  $v_{\text{ave}} \gtrsim 1,000 \text{ km s}^{-1}$ ), which can be readily classified as BALs. Absorbers located in the lower-

<sup>4</sup>  $v_{\text{ave}}$  is the absorption-weighted average velocity, while  $\Delta v$  is the difference between maximum and minimum velocities of the absorption troughs, See Liu et al. 2014 for details.

right corner should fall in the traditional intrinsic NAL category. Considering the velocity zero-point uncertainty of  $\sim 100 \text{ km s}^{-1}$  determined by [O III], [O II], Mg II, and Balmer emission lines (Zhou et al. 2006b; Nestor et al. 2008), absorbers located in the middle part within the two dashed lines can be taken as unshifted, most of which might be of a different origin than the left-hand BAL and NAL outflows. Their relation with those redshifted absorbers located in the lower-right corner is not clear, neither is the nature of the redshifted absorbers (see Shi et al. 2014 for a case study)<sup>5</sup>. With an associated quasar showing an NLS1-like emission line spectrum, the broadest Mg II absorption trough, a common redshift coincidence with that of the quasar emission lines, the same symmetrical velocity structure of all isolated absorption lines, SDSS J0802+5513 is the most extreme case of the unshifted He I\*  $\lambda 3889$  absorbers. Taking advantage of the profuse absorption line spectrum, a detailed study of this extreme case may shed new light on the nature of this mysterious new kind of absorbers. We collected existing photometric data and performed subsequent NUV through optical to NIR spectroscopic follow-ups from 2008 to 2012 using the Blue Channel Spectrographs at the Multiple Mirror Telescope (MMT), the Multi-Object Double Spectrographs (MODS) at the Large Binocular Telescope Large Binocular Telescope (LBT), and TripleSpec at the 200-inch Hale Telescope (P200). The photometric and spectroscopic data are summarized in Table 1 and Table 2, respectively. We show the data in Figure 2 and give them detailed descriptions in next two subsections.

## 2.2. Broad Band Photometry

The photometric data include fluxes at 1.4 GHz by NRAO VLA Sky Survey (NVSS, Condon et al. 1998) and Faint Images of the Radio Sky at Twenty-cm (FIRST, Becker et al. 1995) in the radio; IR magnitudes from the Wide-field Infrared Survey Explorer (WISE; Wright et al. 2010) and the Two Micron All Sky Survey (2MASS, Skrutskie et al. 2006); optical magnitudes from SDSS; and NUV magnitude from the

Galaxy Evolution Explorer (GALEX, Morrissey et al. 2007).

SDSS J0802+5513 has been monitored in Catalina Real-time Transient Survey over 7 year (Drake et al. 2012). The light curve in V band shows no significant variations beyond the intrinsic  $1\text{-}\sigma$  flux scatter of 15% (see Figure 3). The data suggests that the quasar did not show significant variability. As shown in the first panel of Figure 2, the SED of SDSS J0802+5513 is apparently red as compared to a quasar composite. The quasar composite used in the fit is the combination of SDSS optical ( $\lambda \leq 3000 \text{ \AA}$ , Vanden Berk et al. 2001), IRTF NIR ( $3000 \text{ \AA} \leq \lambda \leq 3.5 \text{ }\mu\text{m}$ , Glikman et al. 2006; see Zhou et al. 2010 for an application) and Spitzer MIR to FIR ( $\lambda \geq 3.5 \text{ }\mu\text{m}$ , Netzer et al. 2007) composites. We then estimated reddening of the quasar by fitting the quasar composite spectrum to the SED of SDSS J0802+5513 assuming a Small Magellanic Cloud (SMC) type extinction curve (Lequeux et al. 1982; Cartledge et al. 2005). The best-fitted model is obtained by minimizing  $\chi^2$ . The best-fitted  $E(B - V)$  is 0.36 mag, which agrees well with that indicated by the flux ratios of  $\text{Pa}\beta/\text{H}\alpha$  ( $E(B - V) \sim 0.4$ ) and  $\text{H}\alpha/\text{H}\beta$  ( $E(B - V) \sim 0.3$ ) as detailed in §3.1. It can be seen in the first panel of Figure 2 that this simple model well reproduces the observed SED.

SDSS J0802+5513 is detected by FIRST and NVSS at 1.4 GHz in the radio. No significant variability was observed between the two epochs. Radio loudness, defined as  $R \equiv S_{5 \text{ GHz}}/S_B$ , is 110 and 25, respectively, before and after reddening correction. The NVSS flux at 1.4 GHz was used to estimate the 5 GHz emission  $S_{5 \text{ GHz}}$  and a radio spectral index of  $\alpha_r = 0.5$  ( $S_\nu \propto \nu^{-\alpha_r}$ ) was assumed. We corrected the  $B$  band flux  $S_B$  flux using the best-fitted reddening value. SDSS J0802+5513 is moderately radio-loud, and it becomes radio-intermediate after reddening correction. SDSS J0802+5513 was also observed at 18 cm by the Multi-Element-Radio-Linked Interferometer Network (MERLIN). It is unresolved at  $0''.3$  resolution, corresponding to a linear scale of about 1.6 kpc the redshift of the quasar (Zuther et al. 2012).

## 2.3. Spectroscopy

The SDSS spectrum that we use is the improved sky-residual subtracted version as pub-

<sup>5</sup> The origin of these redshifted absorbers may also be different from the BAL quasars with redshifted troughs identified by Hall et al. (2013), which are much broader and often with blueshifted absorption too.

TABLE 1  
BROAD BAND PHOTOMETRY OF SDSS J0802+5513

band	flux mag/mJy	facility	obs. date (UT)	reference
NUV	22.62±0.26	GALEX	2004-06-05	1
<i>u</i>	20.79±0.06	SDSS	2003-03-11	2
<i>g</i>	19.21±0.02	SDSS	2003-03-11	2
<i>r</i>	18.42±0.01	SDSS	2003-03-11	2
<i>i</i>	17.88±0.02	SDSS	2003-03-11	2
<i>z</i>	17.70±0.02	SDSS	2003-03-11	2
<i>J</i>	16.47±0.10	2MASS	1999-04-27	3
<i>H</i>	15.94±0.13	2MASS	1999-04-27	3
<i>K<sub>s</sub></i>	14.66±0.09	2MASS	1999-04-27	3
<i>w<sub>1</sub></i>	12.93±0.03	WISE	2010-01-10	4
<i>w<sub>2</sub></i>	11.72±0.02	WISE	2010-01-10	4
<i>w<sub>3</sub></i>	8.84±0.03	WISE	2010-01-10	4
<i>w<sub>4</sub></i>	6.46±0.04	WISE	2010-01-10	4
1.4 GHz	7.1±0.5	NVSS	1993-11-23	5
1.4 GHz	6.54±0.14	FIRST	1998-07-17	6

References. — (1) Morrissey et al. 2007; (2) Schneider et al. 2010; (3) Skrutskie et al. 2006; (4) Wright et al. 2010; (5) Condon et al. 1998; (6) Becker et al. 1995.

TABLE 2  
JOURNAL OF SPECTROSCOPIC OBSERVATIONS

wavelength coverage (Å)	slit (arcsec)	resolution $\lambda/\Delta\lambda$	exposure (sec)	telescope/instrument	obs. date UT
3800–9200	3 <sup>a</sup>	2000	4200	SDSS 2.5m	2003-03-24
3200–5200	1	1800	1500	MMT/Blue Channel	2008-03-30
10000–24000	1.1	2500	1200	P200/TripleSpec	2011-10-21
3200–11000	0.8	2500	2400	LBT/MODS	2012-01-29

<sup>a</sup>The SDSS spectrograph is fiber fed with a size of 3'' in diameter.



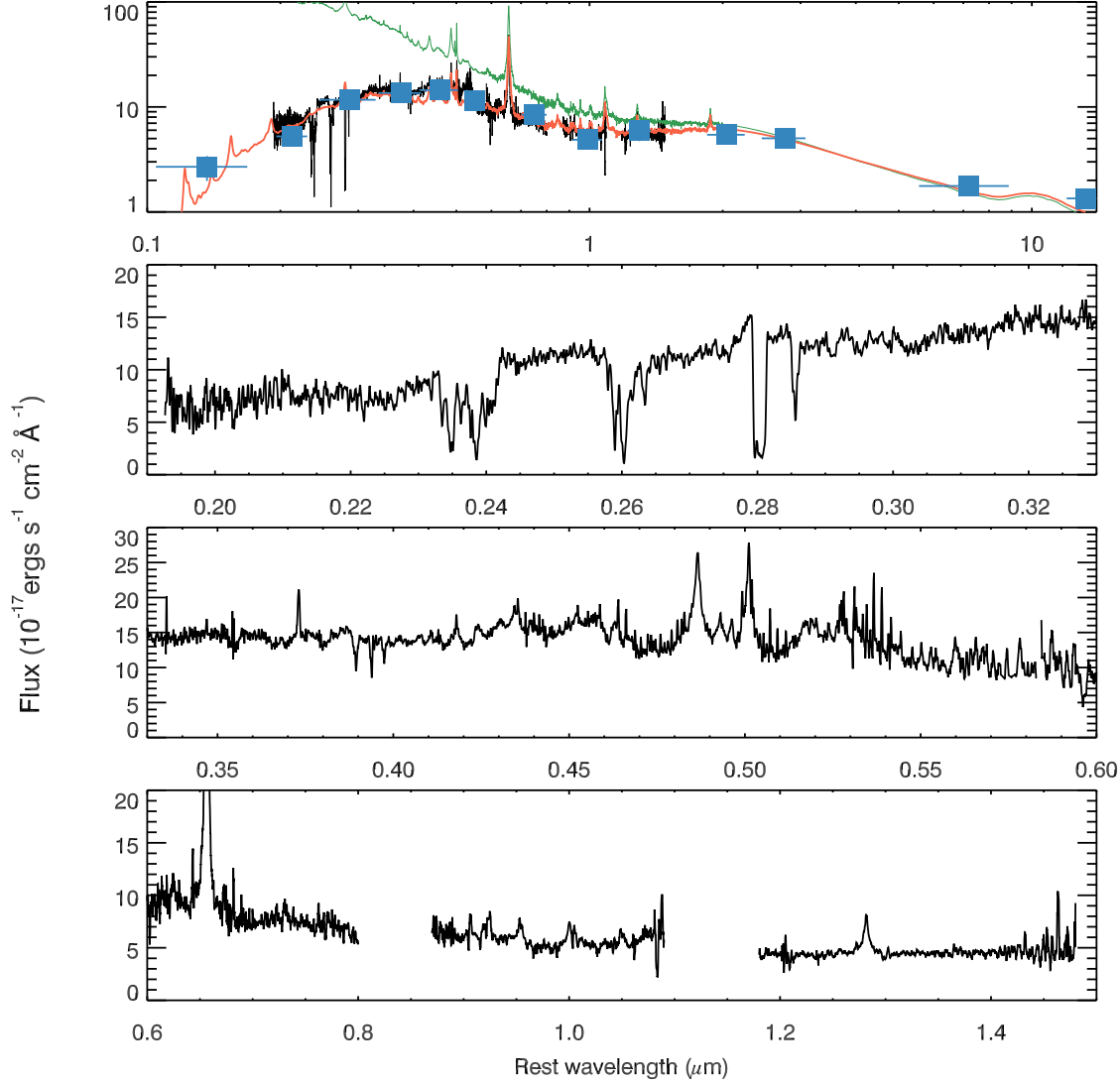


Fig. 2.— In first panel, merged spectrum of SDSS J0802+5513 in the quasar rest-frame is shown in black curve. The data used include SDSS, MMT, LBT and P200 spectroscopy (see Table 2 and § 2.3 for detail), which are smoothed by a boxcar of 7 pixel with bad pixels removed for clarity. A quasar composite spectrum is overplotted in green for comparison. Broad band spectral energy distribution of SDSS J0802+5513 (black squares, photometric data are adopted from GALEX, SDSS, 2MASS and WISE; see Table 1 for detail) is displayed along with the quasar composite reddened by  $E(B - V) = 0.36$  using the SMC-type extinction law (red curve). Expanded views of the merged spectrum are shown in subsequent panels.

lished in Hewett & Wild (2010). To detect any possible absorption line variations and achieve

a higher signal-to-noise ratio (S/N), We carried out a follow-up NUV spectroscopic observation at

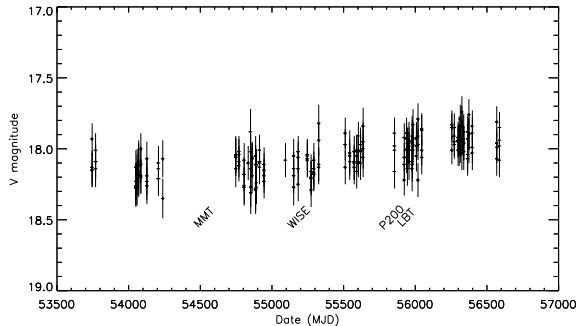


Fig. 3.— Catalina V-band light curve for SDSS J0802+5513. Observing MJDs for all the data are labelled by telescope names, with the exception of SDSS and GALEX, whose observing epochs are not covered by Catalina.

MMT using the blue channel on 2008-03-30. We used the  $1'' \times 180''$  slit and 800 l/mm grating. A total observation time of 1500 s was equally split into two exposures. The seeing during the observation is about  $1.0''$ . He/Ne/Ar lamp is used for wavelength calibration and the KPNO standard star eg182 is observed for flux calibration. We use the standard IRAF package<sup>6</sup> to extract the 1-D spectrum. The extracted spectrum covers a wavelength range of  $\sim 3200$ – $5200$  Å. The median S/N of the MMT spectrum is about  $10 \text{ pixel}^{-1}$  with a resolution of  $R \sim 1800$ , similar to that of SDSS ( $R \sim 2000$ ). Compared to SDSS spectrum, the MMT spectrum shows no significant variations in absorption lines, neither the velocity profiles nor the maximum depths (see §3.2 for detail).

To observe  $H\alpha$  emission line and the expected He I\*  $\lambda 10830$  absorption line, we acquired a NIR spectrum using TripleSpec at P200 telescope via China Telescope Access Program (TAP). The observation was carried out on 2011-10-21 using the standard slit of  $1'' \times 30''$  in A-B-B-A dithering mode. The total exposure time was 1200 s. Using IDL-based Spextool software (Cushing et al. 2004), the raw data are flat-field corrected, telluric corrected (Vacca et al. 2003), wavelength (using sky lines) and flux calibrated. The reduced spec-

trum has a wavelength coverage of  $\sim 1.0$ – $2.4 \mu\text{m}$  and a resolution of  $R \sim 2500$ .

To fill the gap between SDSS and P200 spectra and to detect the possible Na I D absorption doublet, we carried out a follow-up spectroscopy using MODS at LBT with a slit width of  $0''.8$ . Four 600 s exposures were acquired for each of the blue and red channels. CCD reductions, including bias subtraction, flat-field correction were accomplished using Python package “modsCCDRed”. Subsequent reductions are carried out using standard IRAF package. Ne/Hg/Ar/Xe/Kr lamps were used for wavelength calibrations and the standard star Ferge 67 was observed for flux calibration. The extracted LBT spectrum covers a wavelength range of  $\sim 3200$ – $10000$  Å and a resolution of  $R \sim 2500$ . Na I D absorption doublets were not significantly detected on the moderate S/N LBT spectrum.

All above-mentioned spectra were corrected for the Galactic extinction of  $E(B - V) = 0.05$  (Schlegel et al. 1998) assuming an average Galactic ( $R_V = 3.1$ ) extinction law, and transformed into the quasar rest-frame using the redshift of  $z = 0.6640 \pm 0.0005$  as determined by [O II], [S II], Balmer and Paschen emission lines, which is in consistent with that ( $z = 0.6641 \pm 0.0004$ ) given in Hewett & Wild (2010) within errors. Since the quasar SDSS J0802+5513 shows no significant variation in years (see §2.2), we then recalibrated all spectra to photometric data for correcting aperture and seeing effects. We then combined all the spectra, weighted by their S/N, to construct a broad band spectral energy distribution (SED). We display the combined spectrum in the first panel of Figure 2 with expanded views in subsequent panels. It shows narrower Balmer lines and stronger optical Fe II emission lines. [O II] emission is very strong relative high ionization forbidden lines such as [Ne III] and [O III]. Quantitative emission line measurement will be presented in §3.1. Besides emission lines, the absorption spectrum of SDSS J0802+5513 is profuse from rest-frame NUV through optical to NIR. The most prominent absorption features are the strong He I\* line at  $10830$  Å and the blended troughs of Fe II UV1 and UV2 around  $2600$  Å and  $2400$  Å respectively. Identification and measurement of the absorption lines will be described in §3.2.

<sup>6</sup>IRAF is distributed by the National Optical Astronomy Observatory, which is operated by the Association of Universities for Research in Astronomy, Inc., under cooperative agreement with the National Science Foundation.



### 3. Spectral Analysis

#### 3.1. Emission Lines Measurement

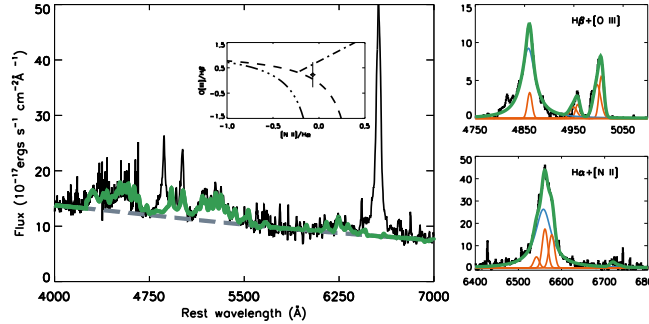


Fig. 4.— Decomposition of the rest-frame optical spectrum of SDSS J0802+5513. In the left panel, the observed pseudo-continuum (black) is modeled by the combination (green) of a power law (dashed gray) and Fe II template. The right panels display the emission line spectrum in the  $H\beta$ + $[O\ III]$  and  $H\alpha$ + $[N\ II]$  regimes after removal of the pseudo-continuum with fitting results overlaid. Narrow forbidden lines are fitted by Gaussian(s), and  $H\alpha$  and  $H\beta$  are fitted by the combination of a Lorentzian and a Gaussian, representing the broad and narrow components, respectively. Observed data are shown in black curves, narrow emission lines in orange, broad lines in blue, and model combinations in green (See §3.1 for detailed description of the models). Diagnostic diagram for narrow line measurements (black diamond with error bars) are shown in the insert of the left panel. Classification lines between LINERs and Seyfert 2 galaxies (Kewley et al. 2006) is shown in dash-dot line, and division between AGNs and star forming galaxies from Kauffmann et al. (2003) and Kewley et al. (2006) in dashed and dotted lines, respectively.

We adopt a fitting method similar to Zhou et al. (2006b) and Dong et al. (2011) to measure the emission lines of interest, with some modifications to accommodate the existence of broad absorption lines. Briefly, the observed spectrum was decomposed into a power law, Fe II emission complex, and emission lines other than Fe II. Given the SED of SDSS J0802+5513 is red, we fit a reddened power law to emission line free windows: 4020–

4050 Å, 4205–4235 Å, 5580–5620 Å, 6350–6400 Å, 6810–6850 Å. Then we subtract the best fitted power law from the observed spectrum, and fit the residual by a Fe II template. We employed the Fe II template built by Véron-Cetty et al. (2004). The template was broadened to fit the Fe II emission strong spectral windows: 4170–4260 Å, 4430–4770 Å, 5080–5500 Å and 6050–6200 Å. The best-fitted model of the pseudo-continuum, including a power law and Fe II multiplets, is shown in the left panel of Figure 4.

Emission lines other than Fe II multiplets were measured by fitting the pseudo-continuum-subtracted spectrum. Each of Balmer and Paschen lines were modeled with two components, a Lorentzian profile for the broad line and a Gaussian for the narrow one. The narrow Balmer and Paschen lines were assumed to have the same width and redshift as that of the low-ionization forbidden lines  $[S\ II]$  and  $[N\ II]$ . All of the narrow emission lines were fitted by a single Gaussian except  $[O\ III]$  doublet, which were fitted with two Gaussians, one for the blue wing (Komossa 2008) and the other for the core of the lines. The width and redshift of  $[O\ III]$  core component were tied to that of low-ionization narrow lines. The doublet ratios of  $[O\ III]$  and  $[N\ II]$  are fixed to their theoretical value 3:1 during the fit. We zoomed in the best-fitted model in  $H\alpha$  and  $H\beta$  regimes in the right panel of Figure 4.

The measured line parameters are summarized in Table 3. In Dong et al. (2008), the authors investigated the broad-line Balmer decrements for an unreddened sample of Seyfert 1 galaxies and QSOs in SDSS and they find that the distribution of the intrinsic broad-line  $H\alpha/H\beta$  ratio can be well described by log-Gaussian, with the peak at  $H\alpha/H\beta=3.06$  and a standard deviation of about 0.03 dex only. The steep broad line ratios of  $H\alpha/H\beta = 4$  in SDSS J0802+5513 thus indicate that the broad line region (BLR) should be significantly reddened. Using  $H\alpha/H\beta$  as the intrinsic Balmer decrement and an SMC type extinction curve, we obtain an estimate of  $E(B - V) = 0.31 \pm 0.05$ . No estimation of intrinsic  $Pa\beta/H\alpha$  is available in (Dong et al. 2008), we assume an intrinsic  $Pa\beta/H\alpha$  ratio of 0.06 as calculated in case B for typical BLR conditions ( i.e.,  $T_e = 10000\ K$  and  $n_e = 10^9\ cm^{-3}$ , Hummer & Storey 1987), we obtain an estimate of  $E(B - V) \approx 0.4 \pm 0.04$ . These

TABLE 3  
RELEVANT EMISSION LINES MEASUREMENT

Transition	Broad line flux $10^{-17}$ ergs cm $^{-2}$ s $^{-1}$	Broad line Width km s $^{-1}$	Narrow line flux $10^{-17}$ ergs cm $^{-2}$ s $^{-1}$	Narrow line Width km s $^{-1}$
Pa $\beta$	230 $\pm$ 20	1800 $\pm$ 170	32 $\pm$ 10	690 $\pm$ 120
H $\alpha$	1946 $\pm$ 28	1800 $\pm$ 170	235 $\pm$ 10	690 $\pm$ 120
H $\beta$	487 $\pm$ 15	1800 $\pm$ 170	40 $\pm$ 15	690 $\pm$ 120
[O II]	...	...	45 $\pm$ 6	690 $\pm$ 120

<sup>a</sup>All quoted errors are statistical ones, widths are FWHMs, the widths of all broad emission lines and narrow lines are tied during the fit, respectively.

agree with the value yielded from SED fitting in §2.2 within errors. The intensity ratios of narrow hydrogen lines are also much steeper than that typically found in the narrow line region (NLR) of AGNs (Zhang et al. 2009) and star-forming galaxies (Xiao et al. 2012 and references therein), suggesting that narrow emission lines might be heavily reddened by interstellar dust clouds as well. However, the relative measurement errors of narrow hydrogen lines are much larger than that of broad lines due to the data quality available. High S/N and resolution spectra are needed to confirm this.

The emission-line properties of SDSS J0802+5513 are typical for an NLS1, with narrow Balmer emission line  $FWHM(H\beta) \approx 1800$  km s $^{-1}$ , strong optical Fe II emission  $R_{4570} \equiv \frac{Fe\ II\ \lambda\lambda 4434-4684}{H\beta} \approx 1$ , and weak [O III] emission  $\frac{[O\ III]}{H\beta} \approx 1.5$ . The black hole mass acquired is  $M_{BH} \approx 2.4 \times 10^8 M_{\odot}$  using the empirical mass-luminosity-line width relation calibrated through reverberation mapping (Peterson & Bentz 2006). In the most conservative case, we integrate the infrared photometries from 2MASS K to WISE w4 to get a lower limit of bolometric luminosity  $L_{bol} = 1.2 \times 10^{46}$  erg s $^{-1}$ . Here we assume the radiation in this wavelength range is from hot dust heated solely by the quasar nucleus given the similar between infrared SED and the quasar composite, and the dust has a full coverage of the central engine. Here we did not include the emission beyond WISE w4. A more reasonable estimate is at least twice the value considering that FIR is not included and covering factor of the dusty torus is about 0.5 based on fraction of

obscured AGNs (e.g. Dong et al. 2005; Hasinger 2008). Alternatively, we can estimate the bolometric luminosity using the monochromatic luminosity of  $\lambda L_{\lambda 5100} \approx 1.8 \times 10^{45}$  erg s $^{-1}$  at 5100 Å. Using the bolometric correction of  $L_{bol}/\lambda L_{\lambda 5100} = 12$  (Richards et al. 2006), the corresponding bolometric luminosity is  $L_{bol} \approx 2.2 \times 10^{46}$  erg s $^{-1}$  and  $L_{bol} \approx 6.4 \times 10^{46}$  erg s $^{-1}$ , respectively, before and after extinction correction. The inferred Eddington ratio is  $\dot{m} \sim 0.4-1.4$ , indicating the central SMBH is undergoing a rapid growth. Assuming a mass-to-energy conversion efficiency of  $\eta = 0.1$ , we inferred a mass accretion rate of  $\dot{M}_{acc} \sim 2.1-7.7 M_{\odot} \text{ yr}^{-1}$ .

### 3.2. Absorption Lines Measurement

#### 3.2.1. Normalization of Absorption Line Spectra

To normalize the absorption line spectrum, absorption-free spectrum of SDSS J0802+5513 must be recovered first. Two technique are commonly adopted to achieve this goal, namely spectral decomposition (e.g. Lu et al. 2008) and template match method (e.g. Zhou et al. 2006a). We split the observed spectrum into three regimes and use different approaches to reconstruct absorption-free spectra, according to the different emission and absorption characteristics. The 3 spectrum regimes of interest are (1) Fe II+Mg II regime (2100–3200 Å), (2) He I\*  $\lambda$ 3889+Ca II regime (3700–4000 Å), and (3) He I\*  $\lambda$ 10830 regime (1–1.4  $\mu$ m). The observed spectrum of the 3 regimes are bloated and displayed in Figure 5 with the best-fitted models overlaid. Identified lines are

labeled by vertical bars on the top of each panel in the Figure and listed in Table 4.

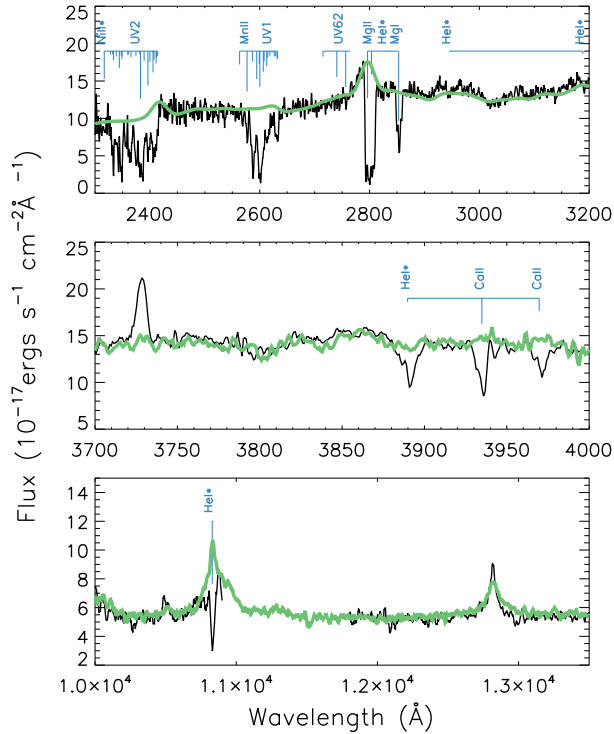


Fig. 5.— Expanded view of the observed spectrum of SDSS J0802+5513 (black) in 3 absorption line regimes of interest overplotted with model absorption-free spectrum (green). Identified transitions are plotted as vertical bars on top of each panel, with the bar lengths proportional to  $\log(gf)$ .

**Fe II+Mg II regime** We employed the spectral decomposition technique for this regime. The observed data were fitted by the combination of three components: a power law, a broadened Fe II+Fe III template and a broad Mg II emission line. The three components were reddened by the same SMC-like dust with  $E(B-V)$  as a free parameter. The Fe II template built by Tsuzuki et al. (2006) is adopted, and the FeIII UV47 multiplet template is from Vestergaard & Wilkes (2001). We assumed that Mg II broad line has the same profile and redshift as Balmer broad lines obtained in §3.1. The best-fitted value of  $E(B-V) \approx 0.30$  is con-

sistent with that inferred from broad band SED fitting ( $E(B-V) \approx 0.36$ , §2.2) and that estimated from broad hydrogen line ratios ( $E(B-V) \approx 0.31-0.4$ , §3.1).

**He I\*  $\lambda 3889$ +Ca II regime** We used the template matching method for this regime due to the fact that emission features in this regime, mainly arising from Fe II, Ti II and Cr II etc., are very complex, and no appropriate templates are available for them (Véron-Cetty et al. 2004, 2006). Furthermore the ratios of optical Fe II multiplets vary dramatically from object to object (Vestergaard & Wilkes 2001), Fe II templates built from in I Zw1 alone cannot fit this region well. We choose the observed spectra of Fe II strong quasars as templates to match the spectrum in this regime. The templates are chosen from DR 7 quasars with  $EW_{\text{FeII } 4570} > 60 \text{ \AA}$  and a median  $S/N > 20$  in [O II] region. The best matched template is the spectrum of SDSS J100446.52+600336.1 (as seen in Figure 5).

**He I\*  $\lambda 10830$  regime** The He I\*  $\lambda 10830$ +Pa $\delta$  emission blends are seriously affected by strong He I\*  $\lambda 10830$  absorption line and the red wing of the blends falls at the gap between J and H bands. As seen in Figure 5, the NIR composite spectrum of quasar derived by Glikman et al. (2006) matches the observed spectrum in this regime quite well.

The detected absorption lines (c.f. Table 4) fall into two categories: relatively isolated lines (Figure 6) and heavily blended lines (Figure 7). The normalized absorption line spectrum is derived by dividing the observed spectrum by the absorption-free spectrum recovered above straightforwardly. This normalization scheme is based on the assumption that the absorption gas covers both the continuum source and BLR of quasar. The validity of such an assumption can be justified by checking the residual flux at the centroid of strong absorption lines. The residual fluxes at the centroids of Mg II, Fe II  $\lambda 2600$  and He I\*  $\lambda 10830$  lines are so small that it would yield negative values at these wavelengths if we subtracted the broad emission lines. This implies that the absorber at least covers a significant part, if not all of the BLR. In this case, the continuum source must be fully covered, since the size of the BLR is about two orders of magnitude larger than that of the accretion disk. Indeed, the apparent optical depth ratios of



### 3.2.2. Measurements of Absorption Lines

We measured the column densities of isolated lines and blended lines using different schemes, respectively.

The isolated He I\*  $\lambda\lambda 3189, 3889$ , Fe II  $\lambda 2586$ , Ca II K, H, and Mg I lines show nearly identical velocity structure as seen in Figure 6. Each line has three distinct components, as indicated by the vertical dashed lines. The deepest component is centered at the quasar systematic redshift. Two shallower components are symmetrically distributed around the deepest one with a velocity shift of  $\Delta v \sim \pm 500 \text{ km s}^{-1}$ . Assuming the background source fully covered and the absorption lines moderately resolved, we evaluated the optical depth profiles of the 6 absorption lines as  $\tau(v) = -\ln I_r(v)$ , where  $I_r$  is the residual intensity of the normalized spectrum. Each of the 6 lines was fitted with 3 Gaussians. The width and centroid of the corresponding Gaussian are tied during the fit. The best-fitted optical depth as a function of velocity is shown in the insert in Figure 7. The equivalent widths ( $EWs$ ) of these 6 lines are measured from the best-fitted models, which are overplotted in Figure 6. We also calculated the column densities of the corresponding lines by integrating their best-fitted apparent optical depth profiles. The measured  $EWs$  and column densities are listed in Table 6. Both of Mg II doublet and He I\*  $\lambda 10830$  lines are seriously saturated and no direct measurement is available. Their absorption troughs are flat-bottomed with residual flux of  $\lesssim 10\%$  at the deepest points<sup>7</sup>. As a conservative estimate, assuming a covering factor of 85%, we rescaled the best-fitted He I\*  $\lambda 3889$  optical depth profile by a factor of 23.3 ( $f\lambda$  ratio of  $\lambda 10830$  to  $\lambda 3889$ , Leighly et al. 2011) to generate a He I\*  $\lambda 10830$  absorption line model. The model is overlaid on the observed data in Figure 6. Mg II  $\lambda 2796$  is seriously blended with Mg II  $\lambda 2803$ , we used the best-guessed  $Mg^+$  column density from photoionization simulation in §4 to create the model overplotted in Figure 6. In Table 5, we take half of the integrated  $EW$  of the blend as a rough estimate for each of the doublet.

<sup>7</sup>Either partially covered background light, scattered light of AGN, or starlight from the host galaxy could contribute to the residual flux. Current available data quality are not of enough to distinguish these possibilities. He I\*  $\lambda 10830$  is seriously affected by sky line residuals.

HiBALs like C IV, Si IV are often much stronger and wider than LoBALs like Mg II, Al III (Zhang et al. 2010; Filiz Ak et al. 2014), it is remarkable that He I\*, Fe II, Ca II and Mg I lines, which are arising from ions with very different ionization potentials, have almost the same velocity structure, and this indicates that SDSS J0802+5513 may have an origin other than traditional BALs. He I\*  $\lambda\lambda 3189, 3889, 10830$  arise from metastable triplet level He I  $2^3S$  at a rather high excitation energy of 19.6 eV. The level is populated by recombination from  $He^+$  ions (Ji et al. 2012), which are created by photons with energies of  $h\nu > 24.56 \text{ eV}$  and are destroyed by photons with  $h\nu > 54.42 \text{ eV}$ . They survive in much different conditions than that of  $Ca^+$  ions and neutral Mg atoms that give rise to Ca II K, H and Mg I lines. Mg atoms are destroyed by photons with  $h\nu > 7.65 \text{ eV}$ ; and  $Ca^+$  ions are created by photons with energies of  $h\nu > 6.11 \text{ eV}$  and are destroyed by photons with  $h\nu > 11.87 \text{ eV}$ . The nearly identical profile of He I\*, Ca II and Mg I lines implies that all of the rest detected absorption lines should have the same velocity structure, because all of them originate from singly ionized ions with surviving conditions in between that of  $He^+$  and of  $Ca^+$  and neutral Mg.

For the Fe II UV1 and UV2 regimes displayed in Figure 7, the absorption lines are too heavily blended to fit them separately. As listed in Figure 4, We identified Fe II lines that arise from ground levels and from excited levels up to  $7955 \text{ cm}^{-1}$ . Ni II\* lines from the excited level of wavelength number  $8395 \text{ cm}^{-1}$  and Mn II lines from the ground level are also identified. All of the identified absorption lines were fitted simultaneously using the same optical depth profile generated above from the isolated lines (shown in the insert of Figure 7). We also calculated  $EWs$  of individual absorption lines by integrating the normalized flux of their models. The best-fitted column densities are summarized in Table 6 and the best-fitted model is compared with the observed absorption line spectrum in Figure 7. This model recovers the observed data very well. This implies that the apparent optical depth (AOD) method, which was adopted to measure the column densities, is reasonable.

As pointed out by Jenkins (1986), large populations of absorption lines can be analyzed col-



TABLE 4  
ABSORPTIONS LINES IDENTIFIED IN SDSSJ0802+5513

Wavelength(Å)	$\log(gf)$	Ion	$E_{\text{low}}$	$g_{\text{low}}$	$E_{\text{up}}$	$g_{\text{up}}$
10830.80	-0.04	He I*	159856	3	169086	9
3889.80	-0.72	He I*	159856	3	185565	9
3188.69	-1.16	He I*	159856	3	191217	9
2852.97	0.270	Mg I	0	1	35051	3
2796.36	0.100	Mg II	0	2	35761	4
2803.54	-0.210	Mg II	0	2	35669	2
3934.83	0.134	Ca II	0	2	25414	4
3969.65	-0.166	Ca II	0	2	25192	2
2576.87	0.433	Mn II	0	7	38807	9
2594.49	0.270	Mn II	0	7	38543	7
2606.46	0.140	Mn II	0	7	38366	5
2344.2139	0.057	Fe II	0	10	42658	8
2374.4612	-0.504	Fe II	0	10	42115	10
2382.7652	0.505	Fe II	0	10	41968	12
2586.6500	-0.161	Fe II	0	10	38660	8
2600.1729	0.378	Fe II	0	10	38459	10
2333.5156	-0.206	Fe II*	385	8	43239	6
2365.5518	-0.402	Fe II*	385	8	42658	8
2389.3582	-0.180	Fe II*	385	8	42237	8
2396.3559	0.362	Fe II*	385	8	42115	10
2599.1465	-0.063	Fe II*	385	8	38859	6
2612.6542	0.004	Fe II*	385	8	38660	8
2626.4511	-0.452	Fe II*	385	8	38459	10
2328.1112	-0.684	Fe II*	668	6	43621	4
2349.0223	-0.269	Fe II*	668	6	43239	6
2381.4887	-0.693	Fe II*	668	6	42658	8
2399.9728	-0.148	Fe II*	668	6	42335	6
2405.6186	0.152	Fe II*	668	6	42237	8
2607.8664	-0.150	Fe II*	668	6	39013	4
2618.3991	-0.519	Fe II*	668	6	38859	6
2632.1081	-0.287	Fe II*	668	6	38660	8
2338.7248	-0.445	Fe II*	863	4	43621	4
2359.8278	-0.566	Fe II*	863	4	43239	6
2405.1638	-0.983	Fe II*	863	4	42440	2
2407.3942	-0.228	Fe II*	863	4	42401	4
2411.2433	-0.076	Fe II*	863	4	42335	6
2614.6051	-0.365	Fe II*	863	4	39109	2
2631.8321	-0.281	Fe II*	863	4	38859	6
2345.0011	-0.514	Fe II*	977	2	43621	4
2411.8023	-0.377	Fe II*	977	2	42440	2
2414.0450	-0.455	Fe II*	977	2	42401	4
2622.4518	-0.951	Fe II*	977	2	39109	2
2629.0777	-0.461	Fe II*	977	2	39013	4
2332.00	-0.720	Fe II*	1873	10	44754	8
2348.81	-0.470	Fe II*	1873	10	44447	8
2360.70	-0.700	Fe II*	1873	10	44233	10
2563.30	-0.050	Fe II*	7955	8	46967	6
2715.22	-0.440	Fe II*	7955	8	44785	6
2740.36	0.240	Fe II*	7955	8	44447	8
2756.56	0.380	Fe II*	7955	8	44233	10
2316.72	0.268	Ni II*	8394	10	51558	8



TABLE 5  
IONIC COLUMN DENSITIES FOR ISOLATED LINES IN SDSS J0802+5513.

Species	transitions	$EW$ ( $\text{\AA}$ )	$N_{\text{ion}}$ ( $\text{cm}^{-2}$ )
Ca II	3969.59	$2.15 \pm 0.16$	$13.59 \pm 0.07$
Ca II	3934.78	$3.52 \pm 0.17$	$13.51 \pm 0.05$
He I*	3889.74	$2.54 \pm 0.18$	$14.73 \pm 0.07$
He I*	3188.66	$0.82 \pm 0.14$	$14.82 \pm 0.17$
Mg I	2852.96	$4.51 \pm 0.53$	$13.53 \pm 0.11$
Mg II	2803.53	$5.82 \pm 0.21^{\text{a}}$	...
He I*	10830.40	$>29.63$	...

<sup>a</sup>Half of the total equivalent width of Mg II doublet absorption lines.

TABLE 6  
IONIC COLUMN DENSITIES FOR THE BLENDED LINES IN SDSS0802+5513.

Species	$E$ ( $\text{cm}^{-1}$ )	$\log_{10} N$ ( $\text{cm}^{-2}$ )
Fe II	0	$14.76 \pm 0.10$
Fe II*	385	$14.11 \pm 0.17$
Fe II*	668	$13.92 \pm 0.29$
Fe II*	863	$13.79 \pm 0.40$
Fe II*	977	$13.52 \pm 0.56$
Fe II*	1873	$15.11 \pm 0.30^{\text{a}}$
Fe II*	7955	$13.27 \pm 1.89$
Fe II	Total	$15.34 \pm 0.5$
Ni II*	8394	$13.85 \pm 0.52$
Mn II	0	$13.31 \pm 0.47$

<sup>a</sup>The column of this level seems strangely large compared to that of ground level, but similar result is seen in QSO 2359-1241, see Korista et al. (2008)

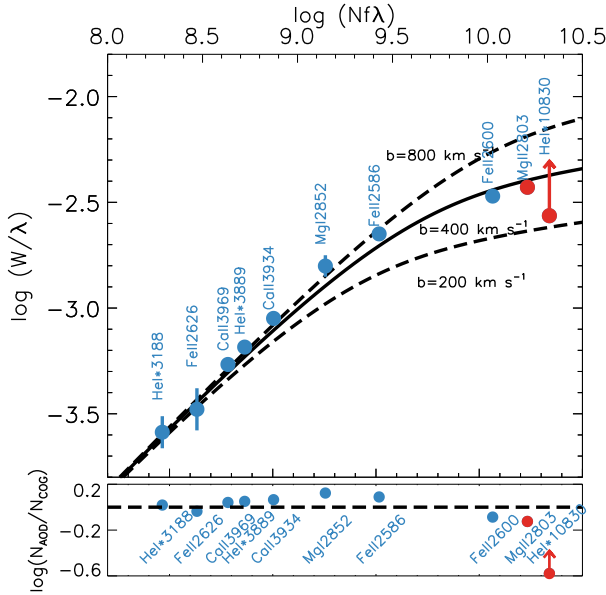


Fig. 8.— Comparison between apparent optical depth (AOD) and curve of growth (COG) analysis. In the upper panel, AOD measurements of isolated lines are shown in blue filled circles (the inferred values of He I\*  $\lambda$ 10830 and Mg II  $\lambda$ 2803 are shown in red. See Figure 6 and 7 for the line measurements.); and the best-fit COG using ground level Fe II lines is shown in filled black curve ( $b = 400 \text{ km s}^{-1}$ ). Also plotted there in dashed black curves are COGs with  $b = 200$  and  $800 \text{ km s}^{-1}$  to guide the eyes. It can be seen in the lower panel that the differences between AOD and COG column density measurements for most ions are less than 0.1 dex.

lectively using the standard, single-component curve of growth (COG) method. We combine the 3 components in SDSS J0802+5513 and perform such single-component COG analysis as a double-check to the AOD measurements. Five Fe II lines with  $gf$  span of about 1 dex (Table 4) were used to evaluate the best-fitted COG. We calculated theoretical COGs of various  $b$  values and searched for the best match the measured  $EW$ s of the ground level Fe II lines. Both of  $b$  and  $N_{\text{Fe II}}$  are free parameters during the fit. The best-fitted COG of Fe II lines is presented in Figure 8.

We interpolated the  $EW$  measurements on the best fitted COG to infer COG column density for other transitions. The differences of column densities evaluated by the AOD and COG methods,  $\log(N_{\text{AOD}}/N_{\text{COG}})$ , are plotted in the lower panel of Figure 8. The differences are negligible within errors, for most lines, in order of 0.1 dex. The AOD method relies on two assumptions: (1) the absorption lines are completely resolved, and (2) the absorber fully covers the background emission source. The overall agreement between  $N_{\text{AOD}}$  and  $N_{\text{COG}}$  indicates that the two assumptions are at least an acceptable approximation.

#### 4. Physical Conditions and Location of the Absorption Gas

In this section, we explore the physical conditions of the absorption gas and locate the gas with the aid of photoionization model calculations and using the column densities of various ions/levels reliably measured in §3.2. Fe II\* absorption lines that arises from excited levels are sensitive to the electron density  $n_e$  (e.g. Arav et al. 2001a; Dunn et al. 2010) in absorbers. Moreover, He I\* lines are a good diagnostics for constraining ionization parameter  $U$ , which is defined as

$$U = \frac{1}{4\pi r^2 n_H c} Q = \frac{1}{4\pi r^2 c n_H} \int_{\nu_0}^{\infty} \frac{L_{\nu}}{h\nu} d\nu, \quad (1)$$

where  $\nu_0$  is the frequency corresponding the hydrogen edge, and  $Q$  is the emission rate of hydrogen ionization photons. Once  $U$  and  $n_e$  are well constrained, the distance of absorption gas can be inferred from Equation (1). We carry out detailed analysis using a photoionization model in §4.1, and discuss in §4.2 the possible dependence on metal abundances, SED of the background quasar, and dust reddening effects. We run photoionization code CLOUDY to carry out the model simulations (version c13.00; c.f. Ferland et al. 1998).

##### 4.1. Basic Model

First we will show that the column density ratio  $N_{\text{Fe II}}/N_{\text{He I*}}$  observed in SDSS J0802+5513 requires the absorber to be thick enough to have a partially-ionized or neutral zone behind the hydrogen ionization front. We started by considering a gas slab with a density of  $n_H$  and a total column density of  $N_H$ , which is illuminated by

quasar radiation (SED from Mathews & Ferland 1987, hereafter MF87). We calculated a grid of models by varying  $U$ ,  $n_{\text{H}}$ , and  $N_{\text{H}}$ , with metallicity fixed to solar abundance. As an example, we plot one result of the model calculations in Figure 9. The ionization structure is shown as a function of the depth parameter  $N_{\text{H}}$  from the illumination surface. Transitions from different ionization state behaves differently in the  $N_{\text{ion}} - N_{\text{H}}$  plane, yielding a sensitive dependence of ion column density ratios on  $N_{\text{H}}$ . This implies that these metal ion column density ratios are good constraints to the absorber thickness. Specifically, only the very narrow  $N_{\text{H}}$  range, labeled by two vertical dashed lines in Figure 9, can produce the value of  $\log(N_{\text{Fe II}}/N_{\text{He I}^*}) = 0.60 \pm 0.35$  observed in SDSS J0802+5513 for the adopted  $U$  and  $n_{\text{H}}$ . This is understandable considering that Fe II (and other singly-ionized metal ions or neutral atoms) and He I\* 2<sup>3</sup>S survive at different conditions.

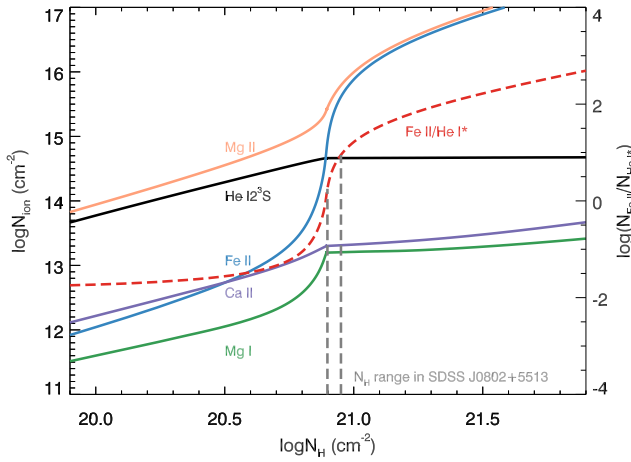


Fig. 9.— Ionic column densities as a function of the depth parameter  $N_{\text{H}}$  for a specific photoionization model with  $U = 10^{-2}$  and  $n_{\text{H}} = 10^5 \text{ cm}^{-3}$ . The incident quasar SED is from Mathews & Ferland (1987, MF87) and a solar abundance is assumed. Note the different behavior of different ions. The sensitive dependence of the column density ratio  $N_{\text{Fe II}}/N_{\text{He I}^*}$  on  $N_{\text{H}}$  (the right-y axis with a different set of tick marks) constrains the total column density of SDSS J0802+5513 to a rather narrow range as labeled by the two vertical dashed lines for the specific model (see §4.1 for the model detail).

He I\* 2<sup>3</sup>S state is mainly populated by the recombination of a  $\text{He}^+$  ion with an electron. As  $N_{\text{H}}$  increases, the main ionization state of helium changes from  $\text{He}^{++}$  to  $\text{He}^+$ , resulting in a sharp increase in He I\* 2<sup>3</sup>S near the ionization front. Further into the cloud, the ionizing photons quickly run out and helium becomes almost neutral, which in turn prevents the generation of He I\* 2<sup>3</sup>S ions. However, the existence of such an ionization front does not prevent the formation of ions with lower ionization potentials, such as Ca II, Mg II and Fe II. As a result,  $N_{\text{Fe II}}/N_{\text{He I}^*}$  continues to increase after the front. Therefore, once the gas abundance and the incident SED are appointed,  $N_{\text{Fe II}}/N_{\text{He I}^*}$  ratio can give a tight constrain to the thickness of the absorber, provided the absorber is thick enough to generate the maximum  $N_{\text{He I}^*}$ . More importantly, this  $N_{\text{He I}^*}$  corresponds to a nearly unique value of  $U$  for a large range of gas density  $n_{\text{H}}$ . As a demonstration, we have run an extensive

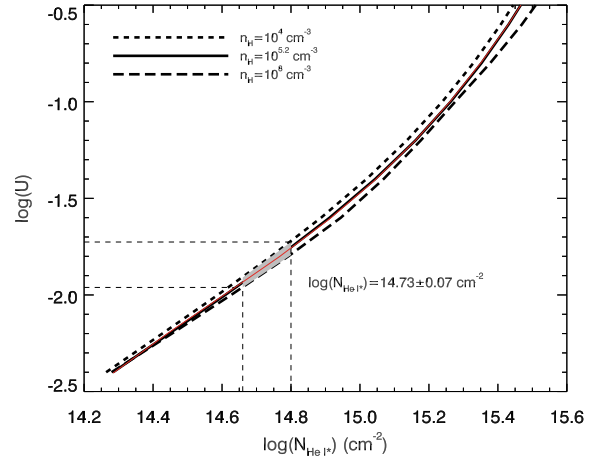


Fig. 10.— Calculated He I\* column densities of the photoionization models with  $n_{\text{H}} \sim 10^4 - 10^8 \text{ cm}^{-3}$  and  $U \sim 10^{-2.5} - 10^0$  (see §4.1 for detail). Note that  $N_{\text{H}}$  is strongly dependent on  $U$  and insensitive to  $n_{\text{H}}$ . The dashed lines indicate the constraint  $U$  range of SDSS J0802+5513.

grid of simulations with  $\log U$  varying from -2.5 to 0 with a step of 0.1 and  $\log n_{\text{H}}$  varying from 4 to 8 with step of 0.2. The upper limit of  $n_{\text{H}}$ ,  $10^8 \text{ cm}^{-3}$ , is determined by the fact that Balmer absorption lines, arising from excited hydrogen  $n=2$  level generated by collision, are not detectable in SDSS

J0802+5513 (Leighly et al. 2011). The lower limit to the density can be set by equilibrium equation of the lowest Fe II excited level  $385\text{ cm}^{-1}$  (de Kool et al. 2001). Using a two-level approximation,

$$n_1 n_e q_{12} = n_2 n_e q_{21} + n_2 A_{21} \quad (2)$$

where the subscripts 1 and 2 represent ground level and the  $375\text{ cm}^{-1}$  level, respectively, and neglecting collisional term, we derive a lower limit of  $n_H \gtrsim 10^4\text{ cm}^{-3}$ . The stop column density of  $N_H = 10^{24}\text{ cm}^{-2}$  is so chosen to enclose a fully developed ionization front for the largest  $U$  concerned<sup>8</sup>. In Figure 10, we show the model prediction of  $N_{\text{He I}^*}$  for a given set of  $U$  and  $n_H$ . The photoionization parameter is constrained to a very narrow range of  $-2.0 \lesssim \log U \lesssim -1.8$  by the observed  $N_{\text{He I}^*}$ <sup>9</sup>. Using the median value of  $\log U = -1.9$ , we calculated the column density ratios of the excited to ground level of  $\text{Fe}^+$  ions as a function of  $n_H$ . Figure 11 presents the results of the  $385\text{ cm}^{-1}$  and  $668\text{ cm}^{-1}$  levels. The estimated density is  $n_H \approx 10^{5.2 \pm 0.3}\text{ cm}^{-3}$ . Measurement uncertainties of higher levels are too large to estimate the electron density reliably. Note that this density is well within the aforementioned value range of  $n_H \sim 10^4\text{--}10^8\text{ cm}^{-3}$ . We recalculated the model using the best estimates of  $\log U = -1.9$  and  $n_H \approx 10^{5.2}\text{ cm}^{-3}$ . The model calculation was stopped at  $N_H = 10^{21}\text{ cm}^{-2}$  where the observed  $N_{\text{Fe II}}$  is reached. The model column densities are compared with the observed values in Figure 13. The observed column densities can be well reproduced by the model for all ions but Ca II, which is slightly under-estimated.

<sup>8</sup>H II region scales approximately as  $\log_{10} N_H \approx 23 + \log U$

<sup>9</sup>The model simulations show an interesting fact that  $N_{\text{He I}^*}$  is strongly dependent on  $U$ , but it is insensitive to  $n_H$ . This suggests that, for the range of model parameters investigated,  $N_{\text{He I}^*}$  could be a good indicator to  $U$ . To a rough approximation ( $\sim 0.1$  dex error), we may neglect the effect of  $n_H$  and adopt the following relation to estimate  $U$  using only  $N_{\text{He I}^*}$ ,

$$\log U = 0.50 - (92.25 - 5.88 \log N_{\text{He I}^*})^{0.5}. \quad (3)$$

This empirical relation is consistent with the model results of well-studied individuals in the literature with He I\* and Fe II\* measurements. E.g., for the intrinsic absorber in QSO 2359–1241, detailed model calculations indicate a range of  $-2.8 \lesssim \log U \lesssim -2.7$  (Arav et al. 2001a), while the result from Equation (3) is  $\log U \approx -2.83$ . See §4.2 for detailed discussion on systematics including incident SEDs, metallicities, and dust reddening effect.

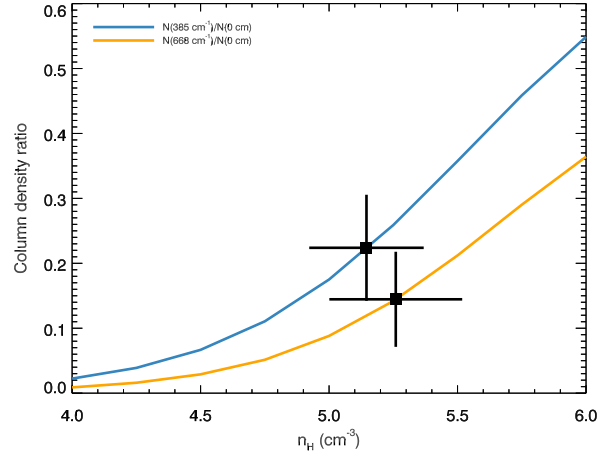


Fig. 11.— Calculated dependence of Fe II excited level populations ( $385\text{ cm}^{-1}$  and  $668\text{ cm}^{-1}$  relative to the ground level as labeled by the legends) on gas density. The measurements are shown as filled squares with  $1\text{-}\sigma$  statistical errors.

We normalized the MF87 SED to the observed luminosity of SDSS J0802+5513 at the WISE w4-band ( $\lambda_{\text{eff}} = 22\text{ }\mu\text{m}$ ), and obtained an estimate of the ionizing photons rate of  $Q_{\text{MF87}} = 2.3 \times 10^{56}\text{ s}^{-1}$ , which should not be affected by reddening. Substituting  $Q_{\text{MF87}}$  and the best evaluates of  $U$  and  $n_H$  into Equation (1), we inferred an estimate to the distance of the absorption gas from the SMBH,  $R \approx 200 (\frac{U}{10^{-1.9}})^{0.5} (\frac{n_e}{10^{5.2}\text{ cm}^{-3}})^{0.5}\text{ pc}$ . The inferred physical thickness of the absorber is  $\Delta R \sim N_H/n_H \approx 0.02\text{ pc}$ , which is rather small compared to its distance from the central engine,  $\Delta R/R \sim 10^{-4}$ .

#### 4.2. Effect of SED, Metallicity, and Dust

Only the MF87 SED and a solar abundance were considered in the basic model described above. Adopting different metallicities or incident SEDs might introduce systematics to model calculations. Neither was dust reddening taken into account in the calculations, and yet it is in fact observed in SDSS J0802+5513. In order to assess these possible systematics, we repeated the calculations adopting different metallicities and incident SEDs, and incorporating the effect of dust (including its effect on heating and cooling in

the photoionized gas, as calculated with Cloudy). Two dust configurations were considered here. (1) Dust is uniformly mixed with the absorption gas. We use the pre-stored abundance set “H II region with grains” offered by CLOUDY as “Orion nebula dust”, which is essentially the average condition of the Orion Nebula (Baldwin et al. 1991; see the note of Table 7). In this case, metals are depleted into dust and the gas phase abundance is sub-solar. (2) The dust is in front of the absorber (a dust screen case). In this case, the dust resides in a very high ionized foreground gas (Dunn et al. 2010), which does not leave imprints on the observed spectra of the quasar but alters the shape the incident continuum. In Figure 12, we show the MF87 SED reddened with  $E(B - V) = 0.36$  using the model extinction curve of “SMC bar” from Weingartner & Draine (2001) since there is no observed extinction curve available in the extreme ultraviolet (EUV). Also displayed in the figure is the standard AGN SED in hazy document (CLOUDY command: AGN T=1.5e5 K, a(ox)=-1.4, a(uv)=-0.5, a(x)=01). This SED has a big blue bump peaked at a lower energy than MF87, and we refer to it as “SOFT SED”.<sup>10</sup>

In all cases,  $U$  and  $N_{\text{H}}$  are adjusted to best match the observed  $N_{\text{Fe II}}$  and  $N_{\text{He I}^*}$ , and  $n_{\text{H}}$  is fixed to be  $10^{5.2} \text{ cm}^{-3}$ . The results are summarized in Table 7 and are compared with observations in Figure 13. It can be seen there that models assuming a solar gas-phase abundance reproduce the observed column densities quite well, while dusty-gas models assuming an intrinsic solar abundance under-estimate  $N_{\text{Ca II}}$  and  $N_{\text{Mg I}}$ . This is expectable, since in these models the gas phase calcium and magnesium are heavily depleted into dust grains. The best-fit models yield  $\text{Ca/H} = -7.7$  and  $\text{Mg/H} = -5.5$ , more than one order of magnitude lower than the solar values. An intrinsic super-solar abundance is needed for the

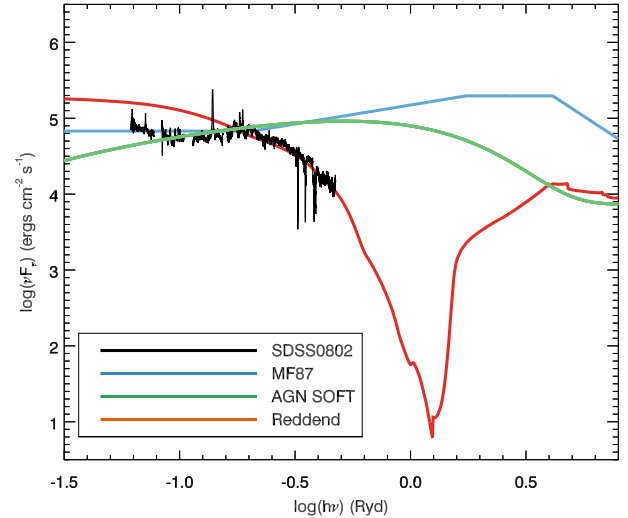


Fig. 12.— Three incident SEDs adopted in the photoionization simulations. The data are normalized to the spectrum of SDSS J0802+5513 at  $\lambda = 5100 \text{ \AA}$  in quasar rest-frame (see §4 for detail).

dusty-gas models to compensate metal depletion. To summarize, all of the acceptable models require  $U \sim 10^{-2} - 10^{-1.5}$  and  $N_{\text{H}} \sim 10^{21} - 10^{21.5} \text{ cm}^{-2}$ . The distances inferred from all models circulated in Table 7 are in the range of  $R \sim 100 - 250 \text{ pc}$ . Dusty-gas models in general require larger  $U$  and accordingly infer a smaller distance compared with dust-free models.

## 5. Origin of the Absorption Gas

The physical conditions and location of the absorption gas are well constrained by analyzing the absorption lines with the aid of photoionization model calculations. It is in the vicinity of the central engine with a distance of hundreds of parsecs. A laminal geometry of the absorber is inferred by comparing the physical thickness ( $\Delta R \sim 0.02 \text{ pc}$ ) with the distance. In addition, the kinematics of the absorption gas is derived by the profile of isolated lines. The centroid of the absorption lines observed in SDSS J0802+5513 perches right at the systematic redshift, and the line profile is almost symmetric in velocity space, spreading from  $\sim -750 \text{ km s}^{-1}$  to  $\sim +750 \text{ km s}^{-1}$ . These infor-

<sup>10</sup>We have also considered cases where ionizing sources are in situ with the gas, e.g. stellar sources. For solar abundance, SEDs from young stellar populations (e.g. 1 Myr SSP from Leitherer et al. 1999) would result in similar results as SOFT SEDs do. In these cases, we cannot use this to infer the distance of gas from the central black hole, so we do not list these results in Table 7 for consistency. Yet the fact itself, that the starburst SEDs could generate observed ionic column density pattern, would fit in our preferred picture of starburst-driven gas flow in SDSS J0802+5513 (see §5 for detail)

TABLE 7  
CLOUDY MODELS

SED <sup>a</sup>	Z	U	N <sub>H</sub>	He I*	Fe II*	Ca II	Mg I	Mn II	Ni II <sup>d</sup>
observation	...	...	...	14.73	15.34	13.59	13.53	13.40	15.34
MF87	HII/DUST <sup>b</sup>	-1.50	21.49	14.75	15.34	11.05	13.00	13.22	13.89
MF87	solar <sup>c</sup>	-1.80	21.21	14.75	15.34	13.07	13.57	13.29	15.11
SOFT	HII/DUST	-1.50	21.46	14.80	15.34	11.35	12.78	13.21	14.11
SOFT	solar	-2.00	20.99	14.62	15.34	13.20	13.47	13.31	15.10
Reddened MF87	solar	-1.3	22.12	14.74	15.34	12.18	13.06	13.26	15.02

<sup>a</sup>MF87: Mathews & Ferland 1987, AGN: CLOUDY command, AGN T = 1.5e5 k, a(ox) = -1.4, a(uv) = -0.5 a(x) = -1.

<sup>b</sup>Abundance set of H II region with dust, see Baldwin et al. (1991) and CLOUDY HAZY documentation.

<sup>c</sup>Abundance set of Solar, see Grevesse & Noels (1993) and CLOUDY HAZY document.

<sup>d</sup>Total Ni II column density is inferred from observed column density of Ni II 8395 cm<sup>-1</sup>, using Boltzmann equation.

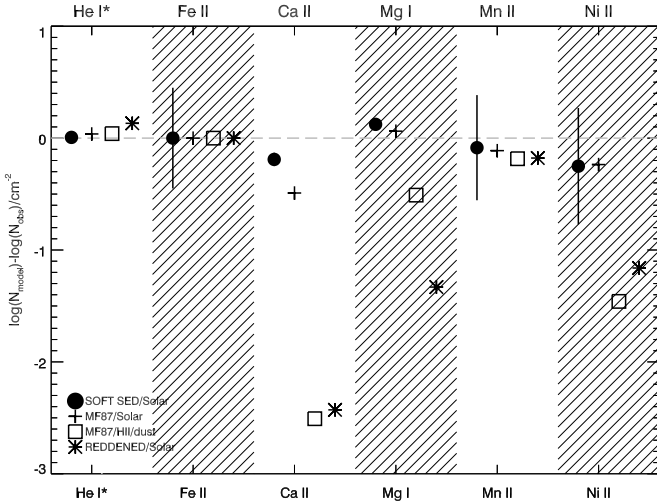


Fig. 13.— Comparison between column density measurements and model calculations (see §4 and Table 7 for the detail). Measurement errors are only shown for the case of SOFT SED for clarity.

mation provides us important clues on the origin of the absorption gas.

The seemingly relatives to SDSS J0802+5513 are iron low-ionization broad absorption line (FeLoBAL) quasars, which are defined by the presence of BALs in excited states of Fe II and/or Fe III, in addition to commonly detected LoBALs, such as Mg II and Al III (e.g. Casebeer et al. 2008). The physical conditions of absorbing gas can be well constrained in a few FeLoBAL quasars, e.g., SDSS J0318-0600 (Bautista et al. 2010; Dunn et al. 2010), SDSS J0838+2955 (Moe et al. 2009), FBQS 0840+3633 (de Kool et al. 2002), QSO 2359-1241 (Bautista et al. 2010; Arav et al. 2001a). The inferred distance of the absorption gas,  $R$ , is typically of sub-kpc or kpc-scale, similar to that of SDSS J0802+5513. Alike thickness in an order of magnitude of  $\Delta R \sim 0.01$  pc is found for these FeLoBAL gas either. Such a laminal geometry,  $\Delta R/R \lesssim 10^{-4}$ , indicates that the absorption gas is generated right at the place it is observed. Because, if the absorber were produced in the immediate vicinity of the central SMBH, it would dissipate long before it arrives at the inferred location due to Kelvin-Helmholtz instability. Therefore the absorption gas of SDSS J0802+5513 should be generated in situ as that



of the well-studied FeLoBAL quasars, the ionized gas of which is a consequence of radiative shocks from interaction of a quasar blast wave with dense interstellar clumps (Faucher-Giguère et al. 2012). However, the FeLoBALs are typically blueshifted by several thousand  $\text{km s}^{-1}$  with respect to the quasar systematic redshifts, unlike what we observed in SDSS J0802+5513. The symmetric line profile is hard to explain by the shock model, since an impact velocity is always needed to induce the shock stress. Although most of traditional BALs do not show the redshifted absorbing trough significantly, Hall et al. (2013) has identified a small sample of longward-of-system BAL quasars, which are somewhat resemblant to the absorption troughs in SDSS J0802+5513. The authors employed high-velocity infalls or rotationally dominated outflows to interpret the rarely observed phenomenon. For individual quasars of the sample (SDSS J101946.08+051523.7 possibly also SDSS J131637.26+003636.0), the absorbers are inferred to have a high density ( $n_e \approx 10^{10.5} \text{ cm}^{-3}$ ) and a small distance ( $R \leq 0.5 \text{ pc}$ ) from the central SMBH, which are very different from that in SDSS J0802+5513 ( $n_e \approx 10^5 \text{ cm}^{-3}$  and  $R \sim 100 - 250 \text{ pc}$ ). Therefore, outflowing mechanism cannot explain the line profile observed in J0802+5513.

Other mechanisms that may drive the absorption gas in SDSS J0802+5513 involve various stellar processes, such as stellar winds, nova or supernova (SN) ejecta. A supernova may cast off gas shells with masses of  $M \gtrsim 1 M_\odot$  to velocities of  $v \sim 10^3 - 10^4 \text{ km s}^{-1}$ , sufficient to produce the expansion velocity of the absorption gas observed in SDSS J0802+5513. Though the masses of nova shells  $M \lesssim 10^{-4} M_\odot$  are much less than that of supernovas, their expansion velocities are typically  $v \sim 10^3 \text{ km s}^{-1}$  (Osterbrock & Ferland 2006), similar to the maximum velocity of the absorption gas of SDSS J0802+5513. Before exploding as supernovas, winds of massive stars can remove more than half of the original mass. To some extreme cases, the terminal velocities of such stellar winds can reach as high as  $v \gtrsim 2 \times 10^3 \text{ km s}^{-1}$ . The typical velocities are a few hundred  $\text{km s}^{-1}$  (Lamers & Cassinelli 1999), within the velocity range of the gas expansion in SDSS J0802+5513. Thus the absorption gas of SDSS J0802+5513 could be generated by the stellar processes in

the circumnuclear starburst rings, which are frequently observed in active galaxies.

An early study of 30 nearby Seyfert galaxies found in their well-resolved images that 57% have inner rings, 43% have outer rings, and  $\sim 30\%$  have both (Simkin et al. 1980). This finding was confirmed by subsequent UV and optical observations of Seyfert 2 galaxies (e.g. González Delgado et al. 1998, 2001; Cid Fernandes et al. 2001, 2004). These observations reveal a typical size of a few hundred pc. About 40% nuclear starbursts are very vigorous ( $L_{\text{SB}} \gtrsim 10^{10} L_\odot$ ) and compact ( $\sim 100 \text{ pc}$ ). A similar conclusion was reached from NIR spectrophotometry of the central  $\sim 300 \text{ pc}$  of 24 Seyfert galaxies (Riffel et al. 2009). The authors found signatures of young stellar populations in 50% of the Seyfert 2 and most of the Seyfert 1 galaxies. Such circumnuclear starbursts were suggested to be directly coupled to the dusty torus, which is the key ingredient of AGN unification schemes (Antonucci 1993; Urry & Padovani 1995). The sizes of circumnuclear starbursts are similar to the estimated distance of the absorption gas in SDSS J0802+5513 ( $R \sim 100 - 250 \text{ pc}$  from the galactic center). Interestingly, the gas-to-dust ratio of  $N(\text{H I})/E(B - V) = 3 - 9 \times 10^{21} \text{ cm}^{-2} \text{ mag}^{-1}$ , as the model evaluations in §4, is close to that of the interstellar medium (ISM) in the Milky Way ( $N(\text{H I})/E(B - V) = 4.8 \times 10^{21} \text{ cm}^{-2} \text{ mag}^{-1}$ , Bohlin et al. 1978). Also the inferred ratio of  $\log N(\text{Ca II})/E(B - V) \approx 14.0$  for the absorption gas in SDSS J0802+5513 is within the range of  $13.3 \lesssim \log N(\text{Ca II})/E(B - V) \lesssim 14.3$  as found in the Galactic ISM. Thus, we propose that the absorption gas in SDSS J0802+5513 coexists with the reddening material, which is very likely the ISM of the host galaxy skirting the dusty torus presumed by AGN unification models. This scenario also explains the rareness of absorption systems like SDSS J0802+5513. The line-of-sight should rightly penetrate the edge of obscuring material, where the radiation from central SMBH is mildly reddened.

Assuming stars are uniformly distributed in the circumnuclear starburst ring, we estimate the in-

falling mass rate induced by stellar process.

$$\begin{aligned}
\dot{M}_{\text{in}} &\sim \frac{M v_{\text{max}}/2}{R} \\
&\sim m_{\text{H}} \times (N_{\text{H}}/2) \times \left(\frac{2\pi R \times H}{R}\right) \times (v_{\text{max}}/2) \\
&\sim 5 M_{\odot} \text{ yr}^{-1},
\end{aligned}
\tag{4}$$

where  $m_{\text{H}} = 1.67 \times 10^{-24}$  g is the proton mass,  $N_{\text{H}} \approx 10^{21} - 10^{21.5} \text{ cm}^{-2}$  is the column density,  $v_{\text{max}} \approx 750 \text{ km s}^{-1}$  the maximum expansion velocity,  $R \approx 100 - 250 \text{ pc}$  the distance, and  $H \approx R$  the “height” of the absorption gas. We estimated  $H \approx R$  assuming that the absorption gas were the periphery of the dusty torus and an absorbed AGN fraction of  $f \sim 50\%$ <sup>11</sup>. Intriguingly enough, such a rough estimate is within the mass accretion rate range of SDSS J0802+5513 inferred in §3.1.

The proposed stellar processes are closely related to ongoing or recent star formation in the host galaxy. As a narrow line quasar, SDSS J0802+5513 may share some common properties with NLS1s, e.g. enhanced star formation (Sani et al. 2010). In Figure 14, we show distribution of [O II] EWs and [O II]/[Ne III] flux ratios for SDSS DR7 quasars. SDSS J0802+5513 has a larger [O II] EW and a higher [O II]/[Ne III] ratio as compared to the bulk of DR7 quasars, indicating possible enhanced star formation in this object. Under the assumption that all the [O II] emission is contributed by star formation, we estimate an upper limit of star formation rate of  $11 M_{\odot} \text{ yr}^{-1}$  using the calibration of Kennicutt (1998) and tried to distinguish different stellar processes, namely stellar winds and supernova explosions.

Several stellar evolution phases can produce energetic stellar winds. Post-main-sequence stars near the ends of their lives often eject large quantities of mass ( $10^{-3} M_{\odot} \text{ yr}^{-1}$ ), but the velocities of those wind are typically  $10 \text{ km s}^{-1}$ , far less than the velocity of gas in SDSS J0802+5513. The terminal velocity of early type stars may meet the velocity requirement, yet with lower mass loss rate. The wind in early type stars is only efficient at high luminosity  $L > 10^4 L_{\odot}$  (Kudritzki & Puls 2000) with a mass

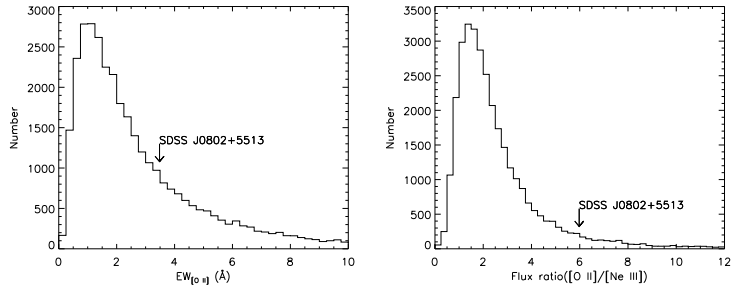


Fig. 14.— Distributions of [O II] EW and [O II]/[Ne III] flux ratio for SDSS DR7 quasars. Values for SDSS J0802+5513 are marked as downward arrows.

loss rate of the order  $10^{-5} M_{\odot} \text{ yr}^{-1}$  or even smaller ( $10^{-7} M_{\odot} \text{ yr}^{-1}$ ) for B stars (Krticka 2014). The corresponding stellar mass should be  $> 20 M_{\odot}$ . To account for the accretion rate,  $5 \times 10^5$  such stars are needed. For a Salpeter initial mass function from  $0.1$  to  $125 M_{\odot}$ , the required  $5 \times 10^5$  massive stars is equivalent to a total stellar mass of  $10^8 M_{\odot}$ . Assuming a typical lifetime of  $1 \text{ Myr}$  for such high mass ( $> 20 M_{\odot}$ ) stars, we can deduce that a star formation rate of  $100 M_{\odot} \text{ yr}^{-1}$  is needed to supply the mass inflow. The required star formation rate is approximately an order of magnitude larger than the observed SFR in SDSS J0802+5513 even assuming all the [O II] emission (see Table 3) is contributed by star formation. It seems that the possibility of stellar winds accretion can be ruled out, although this probably could be the case in AGNs with much lower accretion rate such as Sgr A\* (Cuadra et al. 2006), where a total stellar mass loss rate of  $10^{-3} M_{\odot} \text{ yr}^{-1}$  (Najarro et al. 1997) is sufficient. Either a large amount of obscured star formation (Xiao et al. 2012) exists given the existence of moderate dust extinction in SDSS J0802+5513, or mechanisms other than stellar winds should be invoked.

On the other hand, supernova explosions could inject nearly all the mass of their progenitor into their surroundings and has been proposed to work even at very inner region of AGNs (Wang et al. 2010). SN explosions observed today are related to its past star formation history, in the means that a progenitor with mass  $M_*$  will explode  $t(M_*)$  years later after its formation, with  $t(M_*) = 13(M_*/M_{\odot})^{-2.5}$ . If a constant star

<sup>11</sup>Hasinger (2008) found that the absorbed AGN fraction is  $f \sim 20 - 80\%$  for  $L_{\text{X}} \sim 10^{42} - 10^{46} \text{ erg s}^{-1}$ , and  $f$  increases with decreasing X-ray luminosity  $L_{\text{X}}$

formation rate of  $10 M_{\odot} \text{ yr}^{-1}$  such as in SDSS J0802+5513 holds for the past 100 Myr, i.e. the typical AGN life cycle (Wang et al. 2006), all stars with mass larger than  $7 M_{\odot}$  will explode today. Assuming a Salpeter IMF, a large fraction  $f_c = 0.38$  of star formation mass will be recycled into the ISM (Wang et al. 2010). In the case of SDSS J0802+5513, this adds up to a mass loss rate of  $4 M_{\odot} \text{ yr}^{-1}$ , given its star formation rate of  $10 M_{\odot} \text{ yr}^{-1}$ . It seems that supernova could supply enough gas provided that the star formation in the near past (100 Myr) is at least as intense as what is going on right now in SDSS J0802+5513.

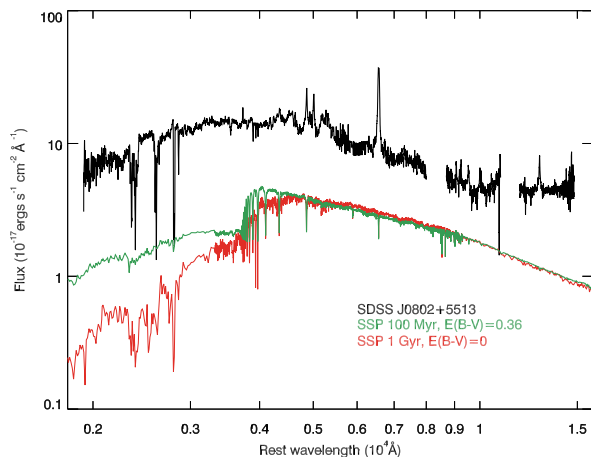


Fig. 15.— Possible stellar populations in SDSS J0802+5513, as constrained by residual flux underneath the saturated absorption troughs of Fe II multiplets UV1, UV2, Mg II doublets and He I  $\lambda 10830$ . Overplotted are SSPs from Bruzual & Charlot (2003), normalized to the flux at  $10830 \text{ \AA}$  of SDSS J0802+5513; a 100 Myr SSP reddened by  $E(B - V) = 0.36$  using SMC-type extinction curve is shown as a green line, while a 1 Gyr SSP as a red line.

Underlying stellar populations in the host galaxies of AGNs could shed light on their past star formation history. It is difficult to extract information of the stellar component for high redshift AGNs as they outshine their hosts. For low redshift AGNs, for example in the quasar He I\* absorber IRAS 14026+4341 (Jiang et al. 2013), Hamilton et al. (2002) measured the brightness of host galaxy by subtracting the nucleus in the high-

resolution image observed by HST/WFPC2<sup>12</sup>, yielding a brightness ratio of host galaxy to nucleus  $\sim 12\%$ . In the case of SDSS J0802+5513, the residual fluxes underneath the flat-bottomed absorption troughs are at similar levels as observed in IRAS 14026+4341. The residual fluxes in multiple wavelengths provide a unique chance to put constraint on the stellar population of the host under the assumption that most of the residual light can be accounted for by the stellar component (Brotherton et al. 1997). Four such troughs are available in SDSS J0802+5513, namely Fe II UV1 and UV2 at  $2600 \text{ \AA}$  and  $2400 \text{ \AA}$ , respectively, Mg II doublet at around  $2800 \text{ \AA}$  and He I\*  $\lambda 10830$ , spanning from NUV to NIR. In Najita et al. (2000), four low-ionization BAL troughs in a reddened BAL quasar F1556+3517, located at  $1860\text{--}2800 \text{ \AA}$  are utilized to put constraint on stellar populations. From the observed upper limit on the strength of the  $4000 \text{ \AA}$  break, the author favors a reddened 50 Myr stellar population over a 1 Gyr one. Besides the evidence proposed in Najita et al. (2000), further constraint can be put on SDSS J0802+5513 with the aid of our new NIR spectroscopy of He I\*  $\lambda 10830$ . As shown in Figure 15, SSPs with ages of 100 Myr and 1 Gyr from Bruzual & Charlot (2003) are normalized to the flux level at the bottom of He I\*  $\lambda 10830$  trough. Although older SSPs can mimic reddened young SSPs in optical–NIR band (i.e. the long-known age-dust degeneracy), the UV flux of older SSPs drops rapidly and fail to fit the UV absorption troughs in SDSS J0802+5513. Using saturated absorption lines as coronagraphs, we inferred that the host galaxy should consist of a significant population of reddened young (several hundred Myr or less) stars, indicating the recent star formation is probably as intense as required for supernova explosion powered winds. The above discussion should be understood with the caveat that, without further observations, we cannot tell if some of the light underneath the absorption trough is contributed by scattered light of the background quasar.

We conclude that supernova explosion seems to be most promising paradigm that drives the gas flow in SDSS J0802+5513 and we will end our discussion with a possible destiny of the gas following

<sup>12</sup>Wide Field Planetary Camera 2

the line of reasoning. While the inflowing gas in SDSS J0802+5513 keeps feeding its central black hole, the outflowing gas would reach the outskirts of its host in 50 Myr, when the host will evolve into a post-starburst galaxy given the estimated age of underlying stellar population. The large scale outflows are ubiquitous in post-starbursts and the origin of these outflows remains a myth, both AGNs and starbursts have been proposed to drive the wind. Study on objects similar to SDSS J0802+5513 could help to resolve the problem.

## 6. Summary and Future Perspectives

We present detailed analysis of SDSS spectrum and newly obtained MMT, P200 and LBT spectra for SDSS J0802+5513. The object is classified as a NLS1 based on the widths of Balmer emission lines and Fe II emission strength. It's moderately dust reddened with an extinction of  $E(B-V) = 0.36$ . Its spectra show rare absorption lines of He I\* and Fe II\*, as well as lines from Ca II, Mg I, Mg II, Ni II and Mn II. The absorption lines show identical profile ranging from  $-750$  to  $750 \text{ km s}^{-1}$ , with its centroid at the same redshift as that determined from emission lines. This object is the first unshifted He I\* min-BAL reported. Extensive photoionization models are calculated using CLOUDY, and He I\* is shown to be a good indicator of ionization parameter. With the aid of the models, the physical parameters of the absorption gas are constrained to be  $\log U \sim -1.8$ ,  $N_{\text{H}} \sim 10^{21} \text{ cm}^{-2}$ ,  $n_{\text{H}} \sim 10^5 \text{ cm}^{-3}$ . The gas is estimated to be  $R \sim 100\text{--}250 \text{ pc}$  away from central black hole. Various origins of the absorption gas are discussed and current observations suggest stellar processes are at work in driving the gas flow. Without further knowledge whether there exists hidden star formation in SDSS J0802+5513, mass losses from stellar winds of high mass stars fail to account for the deduced mass inflowing rate of  $5 M_{\odot} \text{ yr}^{-1}$ . The current data support supernova explosions as the main paradigm funneling the gas in SDSS J0802+5513. Follow-up observations of SDSS J0802+5513 are needed to better study its properties: (1) mid-IR spectroscopies are needed to confirm if there is any hidden star formation, which will put firm constraint on the driving source of the gas flow; (2) polarization observations are needed to see if any polarized (scattered) light exists underneath the absorption trough and

narrow band imaging centered at the absorption troughs will help to constrain the stellar population; (3) High resolution spectroscopies are useful to resolve the heavily blended absorption lines and to improve column density measurements; and 4) X-ray observations are helpful to determine total column density of the absorption gas.

Finally, we note that though very rare, SDSS J0802+5513 has similars. We show the spectra of the 7 unshifted He I\* absorber candidates in Figure 16. Interestingly, all but one (SDSS J130952.89+011950.6) show a red color, like SDSS J0802+5513. Given the ubiquity of star formation ring in low redshift AGNs (Simkin et al. 1980), we might expect to detect much more similar objects than observed. The rarity could have an important implication on the geometry of the absorbers. If the nuclear star formation is co-plane with the dusty torus of quasars, optical spectroscopic surveys like SDSS will have little change to detect such dusty absorbers. Only when our sight lines are coincidentally penetrating the edge of the torus with a moderate optical depth, such as those partially obscured quasars (Dong et al. 2005), can we detect absorbers like SDSS J0802+5513. Studies on these objects could reveal (1) the true nature of quasars with unshifted He I\* absorption lines, (2) their possible connection with partially obscured quasars and (3) the role that starburst driven gas flows play in the coevolution of SMBH and stellar bulges.

This work is supported by the SOC program (CHINARE2012-02-03), the NSFC grant (NSF11033007), National Basic Research Program of China (973 Program, 2013CB834905, 2015CB857005) and Fundamental Research Funds for the Central Universities (WK 2030220010). P.J. acknowledges supports from the National Science Foundation of China with Grants NSFC 11233002 and NSFC11203022, the Fundamental Research Funds for the Central Universities and the China Postdoctoral Science Foundation. Data from NED, NIST and SDSS were used. This research also uses data obtained through the Telescope Access Program (TAP), which is funded by the National Astronomical Observatories, Chinese Academy of Sciences, and the Special Fund for Astronomy from the Ministry of Finance. Observations obtained with the Hale Telescope at

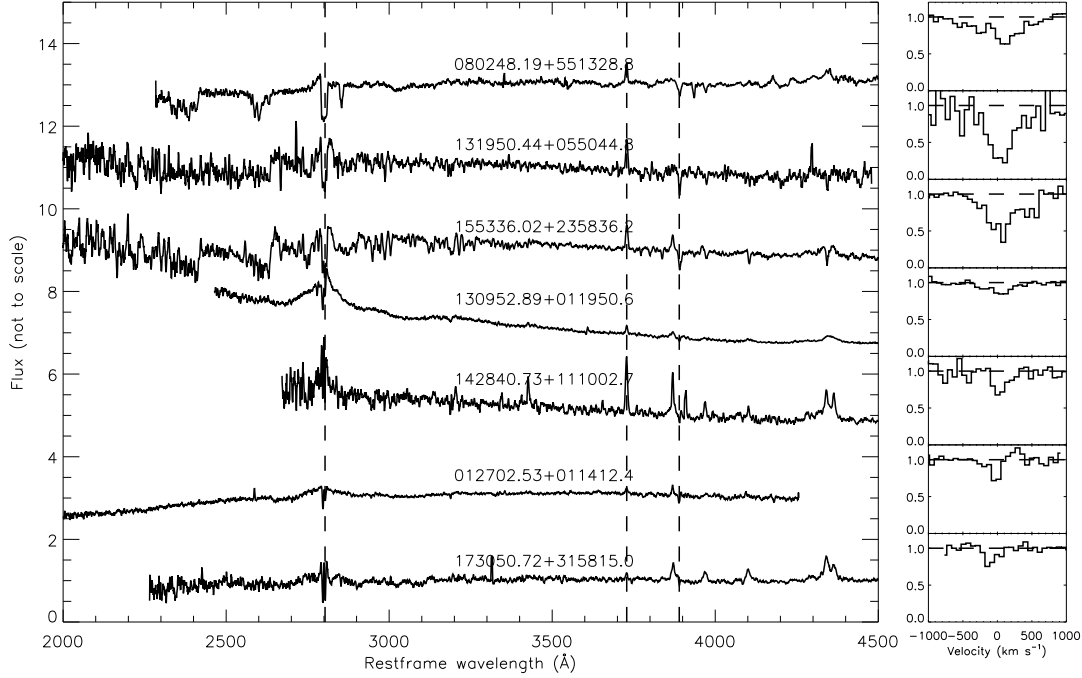


Fig. 16.— SDSS Spectra of unshifted He I\* absorption line quasars. Normalized spectra of He I\*  $\lambda$ 3889 are shown on the right.

Palomar Observatory were obtained as part of an agreement between the National Astronomical Observatories, Chinese Academy of Sciences, and the California Institute of Technology.

## REFERENCES

- Antonucci, R. 1993, *ARA&A*, 31, 473
- Arav, N., Brotherton, M. S., Becker, R. H., Gregg, M. D., White, R. L., Price, T., & Hack, W. 2001a, *ApJ*, 546, 140
- Arav, N., et al. 2001b, *ApJ*, 561, 118
- Baldwin, J. A., Ferland, G. J., Martin, P. G., Corbin, M. R., Cota, S. A., Peterson, B. M., & Slettebak, A. 1991, *ApJ*, 374, 580
- Bautista, M. A., Dunn, J. P., Arav, N., Korista, K. T., Moe, M., & Benn, C. 2010, *ApJ*, 713, 25
- Becker, R. H., White, R. L., & Helfand, D. J. 1995, *ApJ*, 450, 559
- Brotherton, M. S., Tran, H. D., van Breugel, W., Dey, A., & Antonucci, R. 1997, *ApJ*, 487, L113
- Bruzual, G., & Charlot, S. 2003, *MNRAS*, 344, 1000
- Cartledge, S. I. B., et al. 2005, *ApJ*, 630, 355
- Casebeer, D., Baron, E., Leighly, K., Jevremovic, D., & Branch, D. 2008, *ApJ*, 676, 857
- Cid Fernandes, R., Gu, Q., Melnick, J., Terlevich, E., Terlevich, R., Kunth, D., Rodrigues Lac-erda, R., & Jöguet, B. 2004, *MNRAS*, 355, 273
- Cid Fernandes, R., Heckman, T., Schmitt, H., González Delgado, R. M., & Storchi-Bergmann, T. 2001, *ApJ*, 558, 81
- Condon, J. J., Cotton, W. D., Greisen, E. W., Yin, Q. F., Perley, R. A., Taylor, G. B., & Broderick, J. J. 1998, *AJ*, 115, 1693
- Cuadra, J., Nayakshin, S., Springel, V., & Di Mat-teo, T. 2006, *MNRAS*, 366, 358



- Cushing, M. C., Vacca, W. D., & Rayner, J. T. 2004, *PASP*, 116, 362
- Davies, R. 2009, in *Physics of Galactic Nuclei*
- Davies, R. I., Maciejewski, W., Hicks, E. K. S., Tacconi, L. J., Genzel, R., & Engel, H. 2009, *ApJ*, 702, 114
- Davies, R. I., Müller Sánchez, F., Genzel, R., Tacconi, L. J., Hicks, E. K. S., Friedrich, S., & Sternberg, A. 2007, *ApJ*, 671, 1388
- de Kool, M., Korista, K. T., & Arav, N. 2002, *ApJ*, 580, 54
- Dong, X., Wang, T., Wang, J., Yuan, W., Zhou, H., Dai, H., & Zhang, K. 2008, *MNRAS*, 383, 581
- Dong, X.-B., Wang, J.-G., Ho, L. C., Wang, T.-G., Fan, X., Wang, H., Zhou, H., & Yuan, W. 2011, *ApJ*, 736, 86
- Dong, X.-B., Zhou, H.-Y., Wang, T.-G., Wang, J.-X., Li, C., & Zhou, Y.-Y. 2005, *ApJ*, 620, 629
- Drake, A. J., et al. 2012, in *IAU Symposium*, Vol. 285, *IAU Symposium*, ed. E. Griffin, R. Hanisch, & R. Seaman, 306–308
- Dunn, J. P., et al. 2010, *ApJ*, 709, 611
- Faucher-Giguère, C.-A., Quataert, E., & Murray, N. 2012, *MNRAS*, 420, 1347
- Ferland, G. J., Korista, K. T., Verner, D. A., Ferguson, J. W., Kingdon, J. B., & Verner, E. M. 1998, *PASP*, 110, 761
- Filiz Ak, N., et al. 2014, *ApJ*, 791, 88
- Gibson, R. R., et al. 2009, *ApJ*, 692, 758
- Glikman, E., Helfand, D. J., & White, R. L. 2006, *ApJ*, 640, 579
- González Delgado, R. M., Heckman, T., & Leitherer, C. 2001, *ApJ*, 546, 845
- González Delgado, R. M., Heckman, T., Leitherer, C., Meurer, G., Krolik, J., Wilson, A. S., Kinney, A., & Koratkar, A. 1998, *ApJ*, 505, 174
- Granato, G. L., De Zotti, G., Silva, L., Bressan, A., & Danese, L. 2004, *ApJ*, 600, 580
- Grevesse, N., & Noels, A. 1993, *Physica Scripta* Volume T, 47, 133
- Hall, P. B., et al. 2013, *MNRAS*, 434, 222
- Hamann, F., Barlow, T. A., & Junkkarinen, V. 1997, *ApJ*, 478, 87
- Hamilton, T. S., Casertano, S., & Turnshek, D. A. 2002, *ApJ*, 576, 61
- Hasinger, G. 2008, *A&A*, 490, 905
- Hewett, P. C., & Wild, V. 2010, *MNRAS*, 405, 2302
- Hicks, E. K. S., Davies, R. I., Malkan, M. A., Genzel, R., Tacconi, L. J., Müller Sánchez, F., & Sternberg, A. 2009, *ApJ*, 696, 448
- Hummer, D. G., & Storey, P. J. 1987, *MNRAS*, 224, 801
- Jenkins, E. B. 1986, *ApJ*, 304, 739
- Ji, T., Wang, T.-G., Zhou, H.-Y., & Wang, H.-Y. 2012, *Research in Astronomy and Astrophysics*, 12, 369
- Jiang, P., et al. 2013, *AJ*, 145, 157
- Kauffmann, G., et al. 2003, *MNRAS*, 346, 1055
- Kennicutt, Jr., R. C. 1998, *ARA&A*, 36, 189
- Kewley, L. J., Groves, B., Kauffmann, G., & Heckman, T. 2006, *MNRAS*, 372, 961
- Komossa, S. 2008, in *Revista Mexicana de Astronomia y Astrofisica Conference Series*, Vol. 32, *Revista Mexicana de Astronomia y Astrofisica Conference Series*, 86–92
- Komossa, S., Voges, W., Xu, D., Mathur, S., Adorf, H.-M., Lemson, G., Duschl, W. J., & Grupe, D. 2006, *AJ*, 132, 531
- Korista, K. T., Bautista, M. A., Arav, N., Moe, M., Costantini, E., & Benn, C. 2008, *ApJ*, 688, 108
- Krticka, J. 2014, *ArXiv e-prints*
- Kudritzki, R.-P., & Puls, J. 2000, *ARA&A*, 38, 613



- Lamers, H. J. G. L. M., & Cassinelli, J. P. 1999, *Introduction to Stellar Winds*, ed. Lamers, H. J. G. L. M. & Cassinelli, J. P.
- Leighly, K. M., Dietrich, M., & Barber, S. 2011, *ApJ*, 728, 94
- Leighly, K. M., Terndrup, D. M., Baron, E., Lucy, A. B., Dietrich, M., & Gallagher, S. C. 2014, *ApJ*, 788, 123
- Leitherer, C., et al. 1999, *ApJS*, 123, 3
- Lequeux, J., Maurice, E., Prevot-Burnichon, M.-L., Prevot, L., & Rocca-Volmerange, B. 1982, *A&A*, 113, L15
- Liu, W.-J., Zhou, H., & Ji, T. 2014, submitted to *ApJS*
- Lu, H., Wang, T., Yuan, W., Dou, L., Ge, J., Zhou, H., Wang, H., & Dong, X. 2008, *ApJ*, 680, 858
- Mathews, W. G., & Ferland, G. J. 1987, *ApJ*, 323, 456
- Mathur, S. 2000, *MNRAS*, 314, L17
- Meusinger, H., Schalldach, P., Scholz, R.-D., in der Au, A., Newholm, M., de Hoon, A., & Kaminsky, B. 2012, *A&A*, 541, A77
- Misawa, T., Yamada, T., Takada-Hidai, M., Wang, Y., Kashikawa, N., Iye, M., & Tanaka, I. 2003, *AJ*, 125, 1336
- Moe, M., Arav, N., Bautista, M. A., & Korista, K. T. 2009, *ApJ*, 706, 525
- Morrissey, P., et al. 2007, *ApJS*, 173, 682
- Müller Sánchez, F., Davies, R. I., Genzel, R., Tacconi, L. J., Eisenhauer, F., Hicks, E. K. S., Friedrich, S., & Sternberg, A. 2009, *ApJ*, 691, 749
- Najarro, F., Krabbe, A., Genzel, R., Lutz, D., Kudritzki, R. P., & Hillier, D. J. 1997, *A&A*, 325, 700
- Najita, J., Dey, A., & Brotherton, M. 2000, *AJ*, 120, 2859
- Nestor, D., Hamann, F., & Rodriguez Hidalgo, P. 2008, *MNRAS*, 386, 2055
- Netzer, H., et al. 2007, *ApJ*, 666, 806
- Osterbrock, D. E., & Ferland, G. J. 2006, *Astrophysics of gaseous nebulae and active galactic nuclei*
- Osterbrock, D. E., & Pogge, R. W. 1985, *ApJ*, 297, 166
- Peterson, B. M., & Bentz, M. C. 2006, *New A Rev.*, 50, 796
- Richards, G. T., et al. 2006, *ApJS*, 166, 470
- Riffel, R., Pastoriza, M. G., Rodríguez-Ardila, A., & Bonatto, C. 2009, *MNRAS*, 400, 273
- Sani, E., Lutz, D., Risaliti, G., Netzer, H., Gallo, L. C., Trakhtenbrot, B., Sturm, E., & Boller, T. 2010, *MNRAS*, 403, 1246
- Schartmann, M., Meisenheimer, K., Klahr, H., Camenzind, M., Wolf, S., & Henning, T. 2009, *MNRAS*, 393, 759
- Schlegel, D. J., Finkbeiner, D. P., & Davis, M. 1998, *ApJ*, 500, 525
- Schneider, D. P., et al. 2007, *AJ*, 134, 102
- . 2010, *AJ*, 139, 2360
- Shi, X., Zhou, H., Wang, H., Jiang, P., & Ji, T. 2014, submitted to *ApJ*
- Simkin, S. M., Su, H. J., & Schwarz, M. P. 1980, *ApJ*, 237, 404
- Skrutskie, M. F., et al. 2006, *AJ*, 131, 1163
- Tsuzuki, Y., Kawara, K., Yoshii, Y., Oyabu, S., Tanabé, T., & Matsuoka, Y. 2006, *ApJ*, 650, 57
- Urry, C. M., & Padovani, P. 1995, *PASP*, 107, 803
- Vacca, W. D., Cushing, M. C., & Rayner, J. T. 2003, *PASP*, 115, 389
- Vanden Berk, D. E., et al. 2001, *AJ*, 122, 549
- Véron-Cetty, M.-P., Joly, M., & Véron, P. 2004, *A&A*, 417, 515
- Véron-Cetty, M.-P., Joly, M., Véron, P., Boroson, T., Lipari, S., & Ogle, P. 2006, *A&A*, 451, 851

- Vestergaard, M., & Wilkes, B. J. 2001, *ApJS*, 134, 1
- Wada, K. 2004, *Coevolution of Black Holes and Galaxies*, 186
- Wang, J.-M., Chen, Y.-M., & Zhang, F. 2006, *ApJ*, 647, L17
- Wang, J.-M., Yan, C.-S., Gao, H.-Q., Hu, C., Li, Y.-R., & Zhang, S. 2010, *ApJ*, 719, L148
- Weingartner, J. C., & Draine, B. T. 2001, *ApJ*, 548, 296
- Wright, E. L., et al. 2010, *AJ*, 140, 1868
- Xiao, T., Wang, T., Wang, H., Zhou, H., Lu, H., & Dong, X. 2012, *MNRAS*, 421, 486
- York, D. G., et al. 2000, *AJ*, 120, 1579
- Zhang, K., Wang, T.-G., Dong, X.-B., Zhou, H.-Y., & Lu, H.-L. 2009, in *Astronomical Society of the Pacific Conference Series*, Vol. 408, *The Starburst-AGN Connection*, ed. W. Wang, Z. Yang, Z. Luo, & Z. Chen, 281
- Zhang, S., Wang, T.-G., Wang, H., Zhou, H., Dong, X.-B., & Wang, J.-G. 2010, *ApJ*, 714, 367
- Zhou, H., Ge, J., Lu, H., Wang, T., Yuan, W., Jiang, P., & Shan, H. 2010, *ApJ*, 708, 742
- Zhou, H., Wang, T., Wang, H., Wang, J., Yuan, W., & Lu, Y. 2006a, *ApJ*, 639, 716
- Zhou, H., Wang, T., Yuan, W., Lu, H., Dong, X., Wang, J., & Lu, Y. 2006b, *ApJS*, 166, 128
- Zuther, J., Komossa, S., & Zhou, H. 2012, *Journal of Physics Conference Series*, 372, 012005